The Ultraslow Spreading Southwest Indian Ridge

Daniel Sauter

Institut de Physique du Globe de Strasbourg, UMR7516 CNRS-UdS, Ecole et Observatoire des Sciences de la Terre Strasbourg, France

Mathilde Cannat

Laboratoire de Géosciences Marines, CNRS-UMR7097, Institut de Physique du Globe, Paris, France

The Southwest Indian Ridge (SWIR) is among the world's slowest spreading ridges with a full spreading rate of ~14 mm a^{-1} (at 64°E/28°S). The compilation of geophysical and geochemical data along the SWIR reveals a large-scale variation of the density and thermal structure of the axial region. The easternmost part of the SWIR appears to be among the deepest part of the oceanic ridge system, and it is thus inferred to represent a melt-poor end-member for this system. Both the easternmost and westernmost parts of the SWIR reveal a ridge segmentation that differs greatly from what is observed at the faster spreading ridges like the Mid-Atlantic Ridge. The apparent absence of volcanic activity on >100-km-long stretches of the ridge axis, where large expanses of mantle-derived peridotites are exposed in the axial valley, is one of the striking contrasts between the SWIR and these faster spreading ridges. Off-axis geophysical data in the deep magma-poor part of the SWIR reveal a new type of seafloor, which corresponds to thin crust with little to no volcanism. Very large volcanic centers with thick crust occur between these nonvolcanic sections of the ridge and have much higher relief to length ratios than the segments of the MAR. Melt supply appears to be more highly focused beneath these volcanic centers of the SWIR. Melt focusing could result from a combination of melt migration near the base of the lithosphere and rapid melt extraction through dikes rooted in melt-rich regions.

1. INTRODUCTION

It has been known for over 40 years that the thickness of the igneous section of normal oceanic crust is approximately the same in all the world's ocean basins [*Raitt*, 1963]. More recent work has demonstrated that away from the influence of fracture zones (FZs), hotspots and marginal basins, oceanic crust exhibits remarkably uniform crustal thickness, rare earth element concentrations and bulk composition at all but the most slowly spreading ridges [*Bown and White*, 1994]. At full spreading rates below 15–20 mm a^{-1}, all these observed parameters show marked and abrupt changes [*White et al.*, 2001]. Below this critical spreading rate, the melt supply per increment of plate separation is predicted to dramatically decrease [*Reid and Jackson*, 1981]. This is because upwelling velocities in the subaxial mantle are also expected to decrease, leading to a thickening of the thermal boundary

Diversity of Hydrothermal Systems on Slow Spreading Ocean Ridges
Geophysical Monograph Series 188

10.1029/2008GM000843

layer and thereby reducing the height of the melting regime [*White et al.*, 2001]. Changes in ridge geometry, mantle composition, flow, and thermal structure that at faster rates would have a minor effect, dramatically affect crustal production and tectonics at very slow spreading rates [*Cannat et al.*, 2006, 2008a; *Dick et al.*, 2003; *Standish et al.*, 2008]. In particular, amagmatic spreading segments have been proposed to exist on these ultraslow spreading ridges, and it has been argued that these represent a previously unrecognized class of plate boundary structure [*Dick et al.*, 2003].

The Southwest Indian Ridge (SWIR) is a major plate boundary of the world oceans, separating Africa and Antarctica and extending from the Bouvet triple junction (BTJ) in the southern Atlantic ocean to the Rodrigues triple junction (RTJ) in the Indian ocean (55°S/0°40′E and 25°30′S/70°E, respectively, Figure 1). The SWIR is among the world's slowest spreading ridges with a full spreading rate of ~14 mm a^{-1} (at 64°E/28°S) varying only slightly along the 7700-km ridge axis [*Patriat et al.*, 1997; *Chu and Gordon*, 1999]. Together with the Arctic ridges (spreading 6–13 mm a^{-1}), the ultraslow spreading SWIR make up a significant proportion (~10%) of the global oceanic ridge system. In the early 1980s, there was already evidence pointing to significantly thinner crust at ultraslow spreading ridges than along faster spreading ridges [*Reid and Jackson*, 1981]. However, data were sparse for these ultraslow spreading ridges, largely because of logistical issues, both the Arctic Ridge and the SWIR being located in regions, which experience some of the most extreme weather in the world.

High-resolution mapping and sampling of the SWIR began in the 1980s [*Dick et al.*, 1991; *LeRoex et al.*, 1983, 1992; *Mahoney et al.*, 1992; *Munschy and Schlich*, 1990; *Wang and Cochran*, 1995] but were completed only two decades later [*Cannat et al.*, 1999; *Dick et al.*, 2003; *Grindlay et al.*, 1998; *Mendel et al.*, 1997; *Meyzen et al.*, 2003, 2005; *Patriat et al.*, 1997; *Rommevaux-Jestin et al.*, 1997; *Sauter et al.*, 2001; *Standish et al.*, 2008]. Along-axis surveys first revealed striking contrasts between the ultraslow spreading SWIR and faster spreading ridges, the most notable difference being the apparent absence of volcanic activity on long stretches of ridge where large expanses of mantle-derived peridotites are exposed at the seafloor [*Dick et al.*, 2003; *Sauter et al.*, 2004b; *Seyler et al.*, 2003]. The compilation of geophysical and geochemical data along the SWIR also revealed a large-scale variation of the density and thermal structure of the axial region [e.g., *Georgen et al.*, 2001; *Meyzen et al.*, 2003]). The easternmost part of the SWIR was shown to be among the deepest parts of the oceanic ridge system, and it was thus inferred to represent a melt-poor end-member for this ridge system [*Cannat et al.*, 1999, 2008a]. At the same time, seismic data confirmed the occurrence of anomalously thin crust in this easternmost part of the SWIR [*Minshull and White*, 1996; *Minshull et al.*, 2006; *Muller et al.*, 1999].

Limited off-axis geophysical data collected in the late 1990s show very large across- and along-axis crustal thickness variations in the deep magma poor eastern section of the SWIR, suggesting that the melt supply in that part of the ridge is both more focused and shorter lived than at the faster spreading Mid-Atlantic Ridge (MAR) [*Cannat et al.*, 2003]. The first extensive off-axis data set was collected in 2003 with bathymetry, gravity, and magnetic data covering nearly twice the area of Iceland and extending as much as 250 km off axis on both plates (crustal ages to 26 Ma) in the deep easternmost SWIR [*Cannat et al.*, 2006]. This survey area displays the widest expanses known to date of seafloor with no evidence for a volcanic upper crustal layer [*Cannat et al.*, 2006]. This nonvolcanic ocean floor has no equivalent at faster spreading ridges and has been called "smooth seafloor" because it occurs in the form of broad ridges, with a smooth, rounded topography [*Cannat et al.*, 2006]. The easternmost part of the SWIR also contains a large number of corrugated surfaces [*Cannat et al.*, 2006]. Some of these surfaces transition into seafloor that was formed at a lower melt supply, with little to no inferred volcanism [*Cannat et al.*, 2008b, 2009]. This is not the case in the Atlantic, where almost all corrugated surfaces are surrounded by higher melt supply volcanic seafloor [*Escartín and Cannat*, 1999; *Smith et al.*, 2006]. Constant effort was also made during these last two decades to decrypt the record of lower crustal processes in gabbros drilled at Ocean Drilling Program hole 735B on top of an oceanic core complex east of the Atlantis II transform fault (TF 57°E) [*Dick et al.*, 1992, 2000; *Muller et al.*, 1997, 2000]. Hole 735B provides evidence for a strongly heterogeneous lower ocean crust, and for the interplay of deformation, alteration and igneous processes at ultraslow spreading ridges [*Natland and Dick*, 2001]. It is strikingly different from gabbros sampled at faster spreading ridges and at most well-described ophiolite complexes [*Dick et al.*, 2000].

This chapter reviews some of the striking contrasts between the ultraslow spreading SWIR and faster spreading ridges. We begin with a brief description of the physiography of the ridge. We then summarize what is known about the geometry, structure, and evolution of the SWIR, followed by some basic observations that have shaped our understanding of its long-wavelength segmentation. We then focus on the formation and evolution of nonvolcanic seafloor in the westernmost and easternmost parts of the SWIR. Finally, we review possible mechanisms for melt focusing and dis-

tribution along the SWIR. In this chapter, we do not consider the poorly known part of the ridge between the Shaka TF (10°) and the BTJ [*Georgen et al.*, 2001; *LeRoex et al.*, 1983; *Sclater et al.*, 1978] and neither the BTJ [*Brunelli et al.*, 2003; *Ligi et al.*, 1997, 1999; *Mitchell and Livermore*, 1998a, 1998b; *Mitchell et al.*, 2000; *Simonov et al.*, 1996] nor the RTJ areas [*Georgen and Lin*, 2002; *Georgen*, 2008; *Honsho et al.*, 1996; *Kuhn et al.*, 2000; *Mendel et al.*, 2000; *Michard et al.*, 1986; *Mitchell*, 1991a, 1991b; *Mitchell and Parson*, 1993; *Munschy and Schlich*, 1989; *Patriat and*

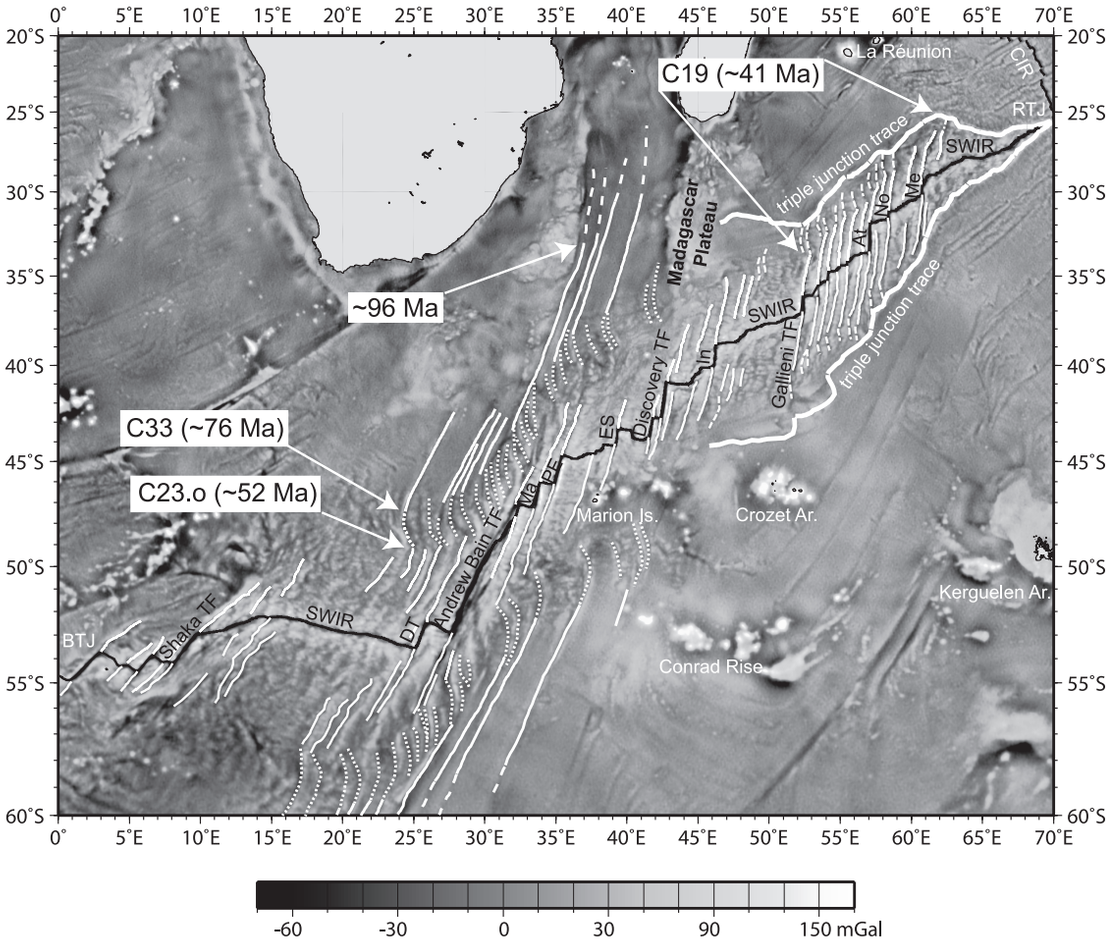

Figure 1. Free-air gravity anomalies over the Southwest Indian Ridge (SWIR) derived from satellite sea-surface altimeter measurements [*Sandwell and Smith*, 1997]. The thin black line indicates the SWIR axis. The eastward progressive variation of the transform fault orientation shows the spreading direction variation along the axis from 45°E at the Bouvet Triple Junction to north-south at the Rodrigues Triple Junction (RTJ) [*Chu and Gordon*, 1999]. The thick white lines indicate the RTJ traces. Thin white lines indicate the fracture zones (FZs) up to ~41 Ma seafloor (magnetic anomaly C19) in the easternmost SWIR and up to ~52 Ma (magnetic anomaly C23.o) in the other part of the SWIR. The last major reorganization of the Indian Ocean spreading system occurred ~41 Ma ago (magnetic anomaly C19). The dashed white lines show the short parts of the FZs, which exhibit a different trend before C19 than at younger ages. They are apparent only near the RTJ because of the relative position of the poles of rotation during this period. A sharp change of spreading direction occurred at the SWIR between C33 and C23.o (dotted white lines) and produced the spectacular twists of the Andrew Bain and other FZs. An age of 96 Ma is estimated for the cusp in the oldest part of the FZs [*Bernard et al.*, 2005]. A marked change in spreading parameters also corresponds to 96 Ma in the Southeast Indian Ocean [*Müller et al.*, 2000]. DT, Du Toit TF; Ma, Marion TF; PE, Prince Edward TF; ES, Eric Simpson TF; In, Indomed TF; At, Atlantis II TF; No, Novara TF; Me, Melville TF; Marion Is., Marion Island; Crozet Ar., Crozet Archipelago; Kerguelen Ar., Kerguelen Archipelago; CIR, Central Indian Ridge.

Courtillot, 1984; *Patriat and Parson*, 1989; *Sauter et al.*, 1997; *West et al.*, 1995].

2. PHYSIOGRAPHY OF THE SOUTHWEST INDIAN RIDGE

The SWIR may be divided into a number of subsections based on changes in the obliquity of the ridge axis (with respect to the normal of the spreading direction) and on the variation of regional axial depths (Figure 1). From the BTJ to 10°E, the SWIR is characterized by closely spaced transform faults [*Sclater et al.*, 1978]. Between the Shaka TF (10°E) and 15°E, the ridge is highly oblique (51°) with a mean depth of ~4000 m ("the oblique supersegment" of *Dick et al.* [2003]). Between 16° and 25°E, a 600-km-long ridge section (the "orthogonal supersegment" of *Dick et al.* [2003]), with a regional depth ~500 m shallower than in the oblique supersegment, is oriented almost perpendicular to the spreading direction [*Grindlay et al.*, 1998]. Further east, the Du Toit, Andrew Bain, Marion, and Prince Edward TFs (25°30′, 30°, 33°30′, 35°30′E, respectively) offset the SWIR by more than 1200 km. The three subsections between the Prince Edward, Discovery, Indomed, and Gallieni TFs (35°30′, 42°, 46°, 52°20′E, respectively) display almost constant and slight overall obliquities (25°) and correspond to a broad bathymetric swell of about 2200 km along axis with an average depth of ~3200 m [*Georgen et al.*, 2001]. The central part of this swell, between the Discovery and Indomed TFs, is somewhat deeper (3600 m) than the neighboring sections. To the east of this swell, axial depths steadily increase, reaching a mean depth of 4730 m in the deepest part of the ridge, between the Melville TF and 69°E close to the RTJ [*Mendel et al.*, 1997]. The ridge section, between the Gallieni and ~64°E, is strongly oblique (>30°) with the Atlantis II, Novara, and Melville TFs (at 57°, 58°24′, 60°45′E, respectively) and nontransform axial discontinuities, which can be traced considerable distances off-axis [*Patriat et al.*, 1997; *Sauter et al.*, 2001]. The ridge section east of ~64° to 67.5°E is only slightly oblique and becomes moderately oblique again near the triple junction. From 61°E to the RTJ, like in the 9°–25°E section, the SWIR is devoid of long-lived transform and nontransform discontinuities [*Cannat et al.*, 2006; *Sauter et al.*, 1997, 2004b].

3. EVOLUTION OF THE SOUTHWEST INDIAN RIDGE

From a kinematic point of view, the SWIR can be divided in two parts, on either side of the uncommonly large offset Andrew Bain/Prince Edward complex FZ system (Figure 1). This spectacular oceanic feature, probably inherited from the Gondwana breakup [*Ben-Avraham et al.*, 1995; *Livermore and Hunter*, 1996; *Ségoufin and Patriat*, 1980], has recorded the whole spreading history of the SWIR [*Bernard et al.*, 2005; *Royer et al.*, 1988]. It has been proposed that it is associated with the diffuse boundary separating the African plate into the Nubian and Somalian new plates [*Chu and Gordon*, 1999; *Horner-Johnson et al.*, 2005, 2007; *Lemaux et al.*, 2002; *Royer et al.*, 2006; *Stamps et al.*, 2008]. The Andrew Bain TF also corresponds to the location of a sharp isotopic transition between Indian- and Atlantic-like mantle sources [*Janney et al.*, 2005; *Mahoney et al.*, 1992; *Meyzen et al.*, 2007].

The reconstructions of the conjugate Mesozoic anomalies [*Eagles and Konig*, 2008; *Marks and Tikku*, 2001] show that the SWIR between Prince Edward and Discovery II FZs is the oldest part of the ridge, spreading since ~155 Ma (magnetic anomaly CM25.y). The present-day "orthogonal supersegment" between 15° and 25° E [*Dick et al.*, 2003] has existed since at least 83 Ma (magnetic anomaly C34y) [*Bergh and Barrett*, 1980]. At that time, the SWIR section to the east of Prince Edward FZ extended up to the Indomed FZ [*Patriat et al.*, 1985]. From that time until now, the axis has lengthened more than 1000 km to the west and more than 2500 km to the east, as the BTJ and the RTJ, driven by faster spreading adjacent ridges, moved to the southwest and the northeast, respectively [*Patriat et al.*, 1997]. The mean velocity of this propagation is ~15 mm a^{-1} toward the southwest, which is equivalent to the present-day opening rate, and 35 mm a^{-1} toward the northeast, which is more than two times faster than this opening rate [*Royer et al.*, 1988]. This dramatic lengthening is the main characteristic of the easternmost and westernmost parts of the SWIR and makes them unique. These parts of the ridge also have the important characteristic of having been initiated entirely in oceanic domains. They thus lack inherited features or geologic complications from early continental breakup [*Patriat and Segoufin*, 1988]. The geometry and segmentation of these parts of the SWIR appear to rather depend on the initial direction of the new segments created at the triple junction and thus on the direction of propagation of the triple junction [*Patriat et al.*, 1997].

As the RTJ migrated northeast between magnetic anomaly C32 (~71 Ma) and magnetic anomaly C23 (~52 Ma), frequent triple junction jumps and changes of configuration resulted in the creation of new SWIR axial discontinuities and produced the highly segmented region of the SWIR from the Gallieni to the Melville TFs [*Dyment*, 1993]. A significant change of spreading direction occurred at the SWIR during this period of complex spreading [*Royer et al.*, 1988] and produced the spectacular twists of the Andrew Bain FZ [*Bernard et al.*, 2005; *McAdoo and Marks*, 1992] (Figure 1). The easternmost part of the SWIR from

the Melville TF to the RTJ has been created after the last major reorganization of the Indian Ocean spreading system at magnetic anomaly C19 (~41 Ma) and is not affected by large offset FZs [*Sclater et al.*, 1981]. At first glance, the smooth curvilinear FZ trends of the highly segmented parts of the SWIR for ages <40 Ma appear consistent with stable plate motion (Figure 1) [*Bernard et al.*, 2005; *Sclater et al.*, 1981], but newly identified magnetic anomalies reveal that a dramatic 50% spreading rate decrease, from slow (30 mm a^{-1}) to ultraslow (15 mm a^{-1}) occurred along the SWIR at magnetic anomaly C6C (~24 Ma) [*Patriat et al.*, 2008]. This last change of spreading rate occurred with a slight change of spreading direction (~13°), which produced local changes of the plate boundary geometry [*Baines et al.*, 2007; *Dick et al.*, 1991; *Sclater et al.*, 2005].

4. LARGE-SCALE VARIATIONS OF MELT SUPPLY ALONG THE SWIR

The compilation of the geophysical and geochemical data along the axial valley of the SWIR reveals large-scale (>200 km) variations in axial depths and Mantle Bouguer Anomalies (MBA) [*Cannat et al.*, 1999; *Georgen et al.*, 2001], *S* wave velocities [*Debayle et al.*, 2005] and in the sodium content of basalts [*Cannat et al.*, 2008a; *Standish et al.*, 2008], which appear primarily to reflect heterogeneities in mantle temperature and/or composition [*Cannat et al.*, 2008a] (Figure 2). Gravity anomalies reflect the density structure of the crust and upper mantle; MBA lows correspond to thicker constant density model crust, or to lighter material, whereas MBA highs correspond to thinner constant density model crust or to denser crustal or upper mantle material. Regional averages for axial depth along long portions (>200 km) of the SWIR are well correlated with axial values of the MBA, averaged over the same regions [*Cannat et al.*, 2008a] (Figure 2). This correlation indicates that regional axial depths do vary with the density structure of the ridge axis and therefore supports the use of these regional depths as indicators of axial crustal thickness and/or mantle temperature. Extracting lateral variations in shear velocity from the surface wave tomography of fundamental and higher mode Rayleigh waves [*Debayle et al.*, 2005] also provides insights into the thermal structure of the upper mantle beneath the SWIR (Figure 2) [*Sauter et al.*, 2009]. Because *S* wave velocities are particularly sensitive to temperature, *S* wave speed maps at shallow depths (e.g., 75 km) are valuable for understanding thermal variations in the upper mantle. Despite some local compositional complexities, regional averages of sodium content of SWIR basalts ($Na_{8.0}$ corrected for the effect of low-pressure fractional crystallization to a common MgO content of 8 wt %) are also well correlated with the regional axial depths along the ridge [*Cannat et al.*, 2008a]. These regional averages of the $Na_{8.0}$ contents of basalts are commonly used to evaluate melt supply variations along the mid-ocean ridge system [*Klein and Langmuir*, 1987].

The Andrew Bain and Gallieni TFs delimit a broad bathymetric swell, which may be further separated in two shallow ridge sections between the Prince Edward and Discovery TFs and between the Indomed and Gallieni TFs. This broad bathymetric swell corresponds to a large MBA negative anomaly indicating thicker constant density model crust or lighter material (Figure 2). MBA values decrease from a high at the Andrew Bain TF to a regional low, between the Prince Edward and Discovery TFs, which is interpreted as due to thicker crust and/or a hotter mantle near Marion hotspot [*Georgen et al.*, 2001]. Further east, MBA values decrease again from a regional high between the Discovery and Indomed TFs to a regional low bounded by the Indomed and Gallieni TFs. This second regional MBA low could result from the interaction of the Crozet hotspot with the SWIR [*Sauter et al.*, 2009]. Sampling the tomographic model of *Debayle et al.* [2005] along the SWIR axis at 75 km depth bring out also two large negative anomalies of *S* wave velocities which are centered near 35°E, close to the Prince Edward TF, and near 50°30′E (Figure 2). We interpret the local fast perturbation in the deeper ridge subsection between the Discovery and Indomed TFs as being a colder region, which separates these two large negative *S* wave anomalies reflecting hotter mantle areas. Between the Andrew Bain TF system and the Gallieni TF, the along-axis variations of $Na_{8.0}$ content of basalts also mimic the axial depth variations (Figure 2): two subsections with a lower mean $Na_{8.0}$ (indicating a higher degree of partial melting in the mantle) are separated by a small subsection between the Discovery and Indomed TFs, where $Na_{8.0}$ is, on average, slightly higher (indicating a lower degree of partial melting).

To the east of Gallieni TF, MBA values increase as the ridge deepens toward the Melville TF and reach their highest values in the easternmost and deepest part of the ridge [*Cannat et al.*, 1999]. Shear wave velocities increase along the oblique ridge subsection east of the Gallieni TF indicating colder mantle beneath these region [*Debayle and Lévêque*, 1997]. Basalt $Na_{8.0}$ content also steadily increases to the east of Gallieni TF (Figure 2), suggesting a progressive eastward decrease of the degree of partial melting in the mantle and, hence, a decrease of the ridge's melt supply. This increase in $Na_{8.0}$ content of basalts is correlated with a decrease in their $Fe_{8.0}$ content [*Meyzen et al.*, 2003]. This is consistent with an eastward decrease in the mean pressure of mantle melting [*Klein and Langmuir*, 1987] and suggests lower mantle temperature in the east [*Meyzen et al.*, 2003]. The lower abundance of volcanic edifices to the east of 62°E also

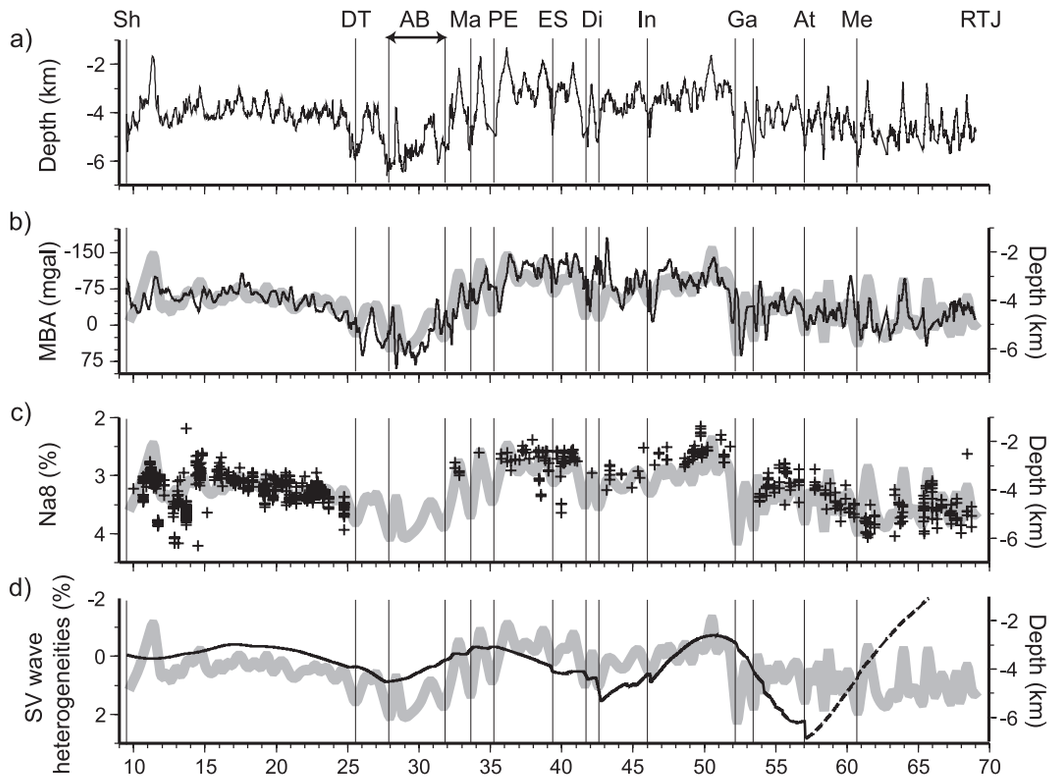

Figure 2. (a) Along-axis depth profile compared to the (b) along-axis variation of the mantle Bouguer anomaly (MBA) [*Georgen et al.*, 2001], to the (c) variation of the $Na_{8.0}$ composition of basalts glasses dredged along the SWIR axis, and to the (d) along-axis variation of the *SV* wave heterogeneity at 75 km depth from the tomographic model of *Debayle et al.* [2005]. The along-axis bathymetric profile was drawn using the multibeam bathymetric data collected during the SWIFT cruise [*Sauter et al.*, 2009], the RODRIGUES cruises [*Munschy and Schlich*, 1990], the CAPSING cruise [*Patriat et al.*, 1997], the Gallieni cruise [*Sauter et al.*, 2001], the KN145L16 cruise [*Grindlay et al.*, 1998], and the KN162 cruise [*Dick et al.*, 2003]. The thick gray line shows a smoothed along-axis depth profile for comparison. The MBA map of *Georgen et al.* [2001] was calculated using the GEBCO-97 bathymetric map (5′ grid spacing) [*Fisher and Goodwillie*, 1997] and satellite-derived free-air anomaly data (2′ grid spacing global gravity database of *Sandwell and Smith* [1997]). MBA values were calculated by subtracting from free-air anomaly data, the gravitational effects of the water-sediment, sediment-crust, and crust-mantle interfaces assuming a constant 5-km-thick reference crust. The densities for seawater, sediment, crust, and mantle are assumed to be 1030, 2300, 2800, and 3300 kg m^{-3}, respectively. The SWIR regional MBA map of *Georgen et al.* [2001] shows similar long-wavelength trends but differs at the shorter-wavelength segment scale from the more reliable local MBA maps calculated with high-resolution multibeam bathymetric data by *Cannat et al.* [1999], [2003], *Grindlay et al.* [1998], *Rommevaux-Jestin et al.* [1997], *Sauter et al.* [2001], [2009]. The along-axis variation of the $Na_{8.0}$ composition of basaltic glasses is from *Cannat et al.* [2008a] and *Standish et al.* [2008] (the subscript 8.0 refers to values corrected for low-pressure fractionation to a common MgO content of 8 wt %, as described by *Klein and Langmuir* [1987]). *SV* wave perturbations are in percent relative to PREM (reference Vs = 4.39 km s^{-1} at 75 km depth) [*Dziewonski and Anderson*, 1981]. To the east of the Atlantis II TF, the *S* waves velocity decreases (dashed line) due to the lack of resolution of the tomographic images and to the influence of the nearby Central and Southeast Indian ridges joining at the RTJ. Sh, Shaka TF; DT, Du Toit TF; AB, Andrew Bain TF; Ma, Marion TF; PE, Prince Edward TF; ES, Eric Simpson TF; Di, Discovery I and II TFs; In, Indomed TF; Ga, Gallieni and Gazelle TFs; At, Atlantis II TF; Me, Melville TF; RTJ, Rodrigues Triple Junction.

suggests a smaller magmatic activity in the easternmost part of the ridge [*Mendel and Sauter*, 1997; *Sauter and Mendel*, 1997].

To the west of Prince Edward TF, the western side of the broad bathymetric swell is marked by a succession of large transform faults (Prince Edward, Marion, Andrew Bain, and Du Toit TFs), with deep transform valleys, which correspond to very high positive MBA values and to a strong increase of *S* wave velocities. From the Du Toit TF up to 17°E, MBA values and shear wave velocities gradually decrease and reach a more or less constant level (Figure 2). $Fe_{8.0}$ on the orthogonal supersegment (16° to 25°E) increases slightly from east to west with the majority of the lavas having higher values than lavas on the oblique supersegment (Shaka TF to 15°E) [*Standish et al.*, 2008]. In contrast to $Fe_{8.0}$, the orthogonal supersegment lavas $Na_{8.0}$ show a small but systematic decrease from east to west, consistent with the evidence for slightly greater melt production and somewhat thicker crust to the west [*Standish et al.*, 2008]. Basalt $Na_{8.0}$ and axial depths both suggest that the orthogonal supersegment has an intermediate regional melt supply higher than the melt supply in the easternmost magma-poor part, and lower than the melt supply in the central part of the ridge with the thickest crust and hotter mantle.

SWIR values for regional axial depth and basalt $Na_{8.0}$ content are consistent with values obtained by a one-dimensional (1-D) analytical model of mantle melting derived from *Langmuir et al.* [1992], which takes into account the effect of upper mantle conductive cooling at the top of the melting regime in a similar way to the corner flow 2-D model of *Bown and White* [1994] (see *Cannat et al.* [2004] for a complete description of the model). The correlation between SWIR lavas and regional depths can be reproduced quite closely by along-axis variations in melt supply, producing a magmatic crust, whose thickness ranges from ~6 km in the shallowest part of the SWIR to only 2 to 3 km in the easternmost and deepest regions [*Cannat et al.*, 2008a] (Figure 3). These latter values are of the same order or smaller than the average seismic crustal thickness of ~3.5 km determined near 66°E [*Minshull et al.*, 2006; *Muller et al.*, 1999]. This large-scale variation of the ridge's melt supply could be explained by a change of about 60°C in the temperature of the subaxial mantle from the central part of the ridge, under the influence of the Marion and Crozet hot spots, to the easternmost SWIR [*Cannat et al.*, 1999], consistent with the broad geoid high observed over the same area. Very low degrees of melting of abyssal peridotites were also inferred from the Cr/(Cr + Al) ratio in spinels along the 61°–64°E section of the SWIR [*Seyler et al.*, 2003]. The along-axis variations of other geochemical proxies for the extent of partial melting, such as Sm/Yb or CaO/Al_2O_3, also support higher mantle temperatures in the subaxial mantle west of Gallieni TF [*Font et al.*, 2007; *Meyzen et al.*, 2003].

The 4–7 mm a^{-1} range of effective spreading rate (the half spreading rate resolved in the ridge-perpendicular direction) along the SWIR falls within the critical range of spreading rates for which mantle uprising beneath the ridge departs from the adiabatic decompression model [see *White et al.*, 2001, Figure 24]. The *Bown and White* [1994] model of corner flow with a spreading rate-dependent lithosphere wedge angle and the corner flow model of *Reid and Jackson* [1981] analogous to the *Phipps Morgan et al.* [1987] model are two end-members in terms of the relationship between spreading rate and melt production (Figure 3). The difference between these end-member models is that mantle upwelling is focused, and therefore accelerated, beneath the ridge in the *Bown and White* [1994] model, while mantle upwelling velocity is nearly equal to the effective spreading rate in the corner flow model of *Reid and Jackson* [1981]. The two models differ widely in their prediction of the total melt thickness deficit due to nonadiabatic mantle cooling at ultraslow effective spreading rates. For a normal temperature mantle and an effective spreading rate of 4 mm a^{-1}, this predicted deficit is about 2 km in the focused mantle upwelling model and about 5 km in the unfocused mantle upwelling model [*Cannat et al.*, 2008a]. The unfocused mantle upwelling model predicts that the central region of the SWIR has a very hot (and/or extremely fertile) mantle, while the easternmost part of the SWIR, would have nearly "normal" mantle temperatures (Figure 3). This would indicate a very broad zone of influence of the Marion-Crozet plume material along the ridge, which is inconsistent with the other geophysical and geochemical data. As already shown by *White et al.* [2001], the unfocused mantle upwelling model also predicts anomalously high mantle temperatures for the global compilation of seismic crustal thicknesses determined at slow spreading oceanic ridges (Figure 3). *Cannat et al.* [2008a] therefore favored the alternative, focused mantle upwelling model in which the central SWIR regions have nearly "normal" to slightly elevated mantle temperatures and in which thin crust in the eastern regions of the SWIR is primarily caused by low initial mantle temperatures.

Using these models of mantle melting to relate regional melt supply to mantle temperature relies on the assumption that the mantle source is chemically and mineralogically homogeneous at the regional scale. These models usually consider the presence of only one lithology (peridodite) in the mantle, but mantle compositional heterogeneities may also contribute to large-scale changes in melt productivity [*Niu and O'Hara*, 2008]. It has been shown that a component other than peridotite is required to explain the isotopic variations of basalts at two segments of the SWIR [*Salters*

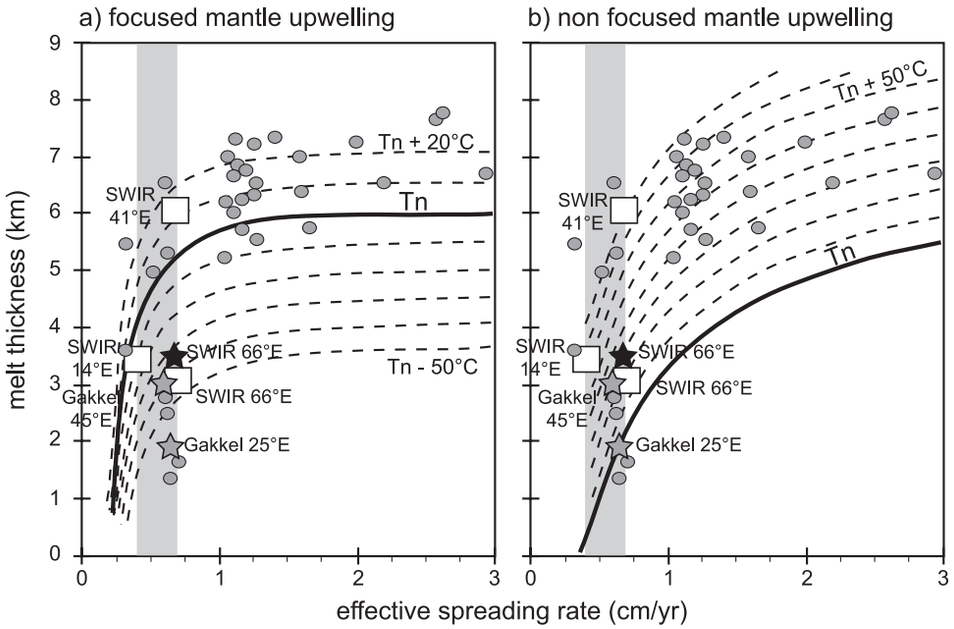

Figure 3. Sketches showing two end-member models for the relationship between melt supply and effective spreading rate (the half spreading rate resolved in the ridge-perpendicular direction) [after *Cannat et al.*, 2008a]. The difference between these end-member models is that in (a) the *Bown and White* [1994] model, the mantle upwelling is focused and therefore accelerated beneath the ridge, while in (b) the corner flow model of *Reid and Jackson* [1981], the mantle upwelling velocity is nearly equal to the effective spreading rate. In the *Bown and White* [1994] model (Figure 3a), melt thickness remains unaffected down to very slow effective spreading rate, at which point it decreases abruptly, whereas in the *Reid and Jackson* [1981] model (Figure b), melt thickness decreases gradually at effective spreading rate less than 3 cm a^{-1}. Bold curves correspond to "normal mantle temperature" (Tn) (corresponding to the production of a melt thickness of 6 km in adiabatic conditions). Shaded domains show the range of effective spreading rate along the SWIR. Open squares indicate the melt supply at 14°E (the oblique supersegment), 41°E (near Marion hot spot), and 66°E (the easternmost deep section). This melt supply is expressed as the thickness of melt produced per increment of spreading and is calculated using a one-dimensional (1-D) analytical model of mantle melting derived from *Langmuir et al.* [1992] (see *Cannat et al.* [2008a] and *Cannat et al.* [2004] for further details). Black star is seismic crustal thickness average at the SWIR near 66°E [*Muller et al.*, 1999]. Gray stars are seismic crustal thickness averages in the eastern part of the Gakkel Ridge [*Jokat et al.*, 2003]. Gray dots are a global compilation of seismic crustal thickness in slow spreading oceans [*Bown and White*, 1994].

and Dick, 2002]. The chemical variability of $K_{8.0}/Ti_{8.0}$ along the 9°–16°E portion of the SWIR also requires a two-lithology mantle source containing a limited (<5%) proportion of mafic material within the ambient asthenosphere [*Standish et al.*, 2008]. Basalts from the easternmost SWIR have also very specific compositions [with depleted heavy rare earth elements and anomalously low Ti8.0 contents with respect to the global Na8.0-Ti8.0 mid-ocean ridge basalt (MORB) array] [*Meyzen et al.*, 2003], while most basalts from the region 10°–14°E [*LeRoex et al.*, 1992; *Standish et al.*, 2008] and 39°–41° (Bezos et al., manuscript in preparation, 2009) are enriched. Mantle spinel lherzolites and harzburgites dredged between 52° and 68°E also show that the residual mantle beneath the easternmost deep SWIR is strongly heterogeneous [*Seyler et al.*, 2003, 2004]. In this portion of the SWIR, the compositional features of the peridotites are certainly in relation with extremely low degrees of melting [*Seyler et al.*, 2003]. In such an environment, initial heterogeneity of the mantle source may have a considerable influence on the melting regime, resulting in enhanced compositional variations in the subaxial mantle at small scales [*Seyler et al.*, 2003; *Standish et al.*, 2008]. Results of the models of mantle melting in the easternmost and westernmost portions of the SWIR should thus be treated with caution but are reliable in the other parts of the SWIR, where normal MORB have been dredged.

5. FOCUSED MAGMATISM VERSUS NONVOLCANIC SPREADING SEGMENTS ALONG THE SWIR AXIS

Both the easternmost and westernmost parts of the SWIR (to the east of the Melville TF and in the oblique supersegment, respectively) reveal a ridge segmentation that differs widely from what is observed at faster spreading ridges such as the MAR. There, high-relief ridge segments (>3000 m high) are linked by >100-km-long, deep axial sections with the apparent absence of volcanic activity [*Dick et al.*, 2003; *Sauter et al.*, 2004b]. Seafloor reflectivity images from the easternmost part of the ridge reveal fresh-looking volcanic terrains in the segments separated by sedimented and highly tectonized terrains along the deep sections of the axial valley [*Gomez et al.*, 2006; *Parson et al.*, 1997; *Sauter and Mendel*, 1997; *Sauter et al.*, 2004b] (Figure 4). Dredging the axial valley revealed that these deep ridge sections are associated with extensive axial outcrops of serpentinized mantle-derived peridotites [*Dick et al.*, 2003; *Mével et al.*, 1997; *Seyler et al.*, 2003] (Figure 5). They were termed "amagmatic" by *Dick et al.* [2003] to reflect this abundance of peridotites and the scattered basalt, minimal diabase, and gabbro recovered in these areas [*Seyler et al.*, 2003; *Standish et al.*, 2008].

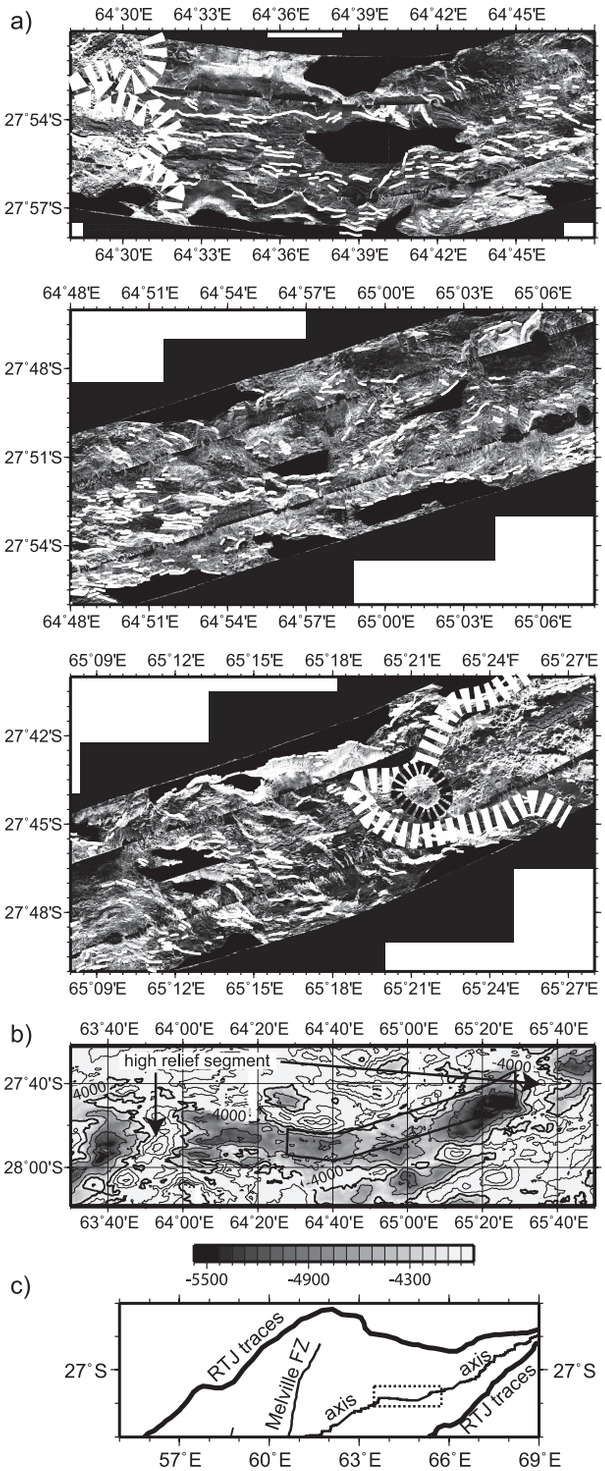

Figure 4. (opposite) Towed ocean bottom instrument (TOBI) side-scan sonar images of the SWIR axial valley between 64°30′E and 65°30′E (a). Thick dashed white lines indicate the sharp contact between fresh-looking volcanic areas (to the west of 64°31′E and to the east of 65°20′E) and sedimented and strongly tectonized areas. Thin white lines indicate faults. The volcanic texture on the TOBI imagery correspond mainly to large conglomerations of subcircular mounds, individually with <500 m diameters (hummocky texture) which can be most readily attributed to individual pillow lava flows. This type of volcanic edifice is the most abundant whereas flat-topped seamounts (see one example shown by the thick black dashed line at 65°21′E) are rare in the axial valley. Sediment causes a lower amplitude return (dark parts of the images) because of acoustic penetration and attenuation in the subsurface, whereas fresh-looking volcanic areas are strongly backscattering (bright areas). Relicts of volcanic edifices are rarely identified in the 82-km-long section between 64°31′ and 65°20′E. This ridge section displays basement blocks which are commonly tectonized and, in some cases, completely dismembered. Although such a long tectonized section has not been recognized at faster spreading ridges, an equivalent side-scan sonar texture has been described by *Parson et al.* [2000, Figure 3g] and *Gràcia et al.* [2000, Figure 3] on TOBI images of smaller nontransform offsets of the MAR where upper mantle and lower crustal rocks are exhumed. See *Sauter et al.* [2004b] for a more detailed mapping of the area. (b) Bathymetric map between the two high relief segments located at 63°55′ and 65°36′E. The black frame indicates the area covered by the TOBI images shown in Figure 4a. (c) Location of this bathymetric map shown by a dotted frame.

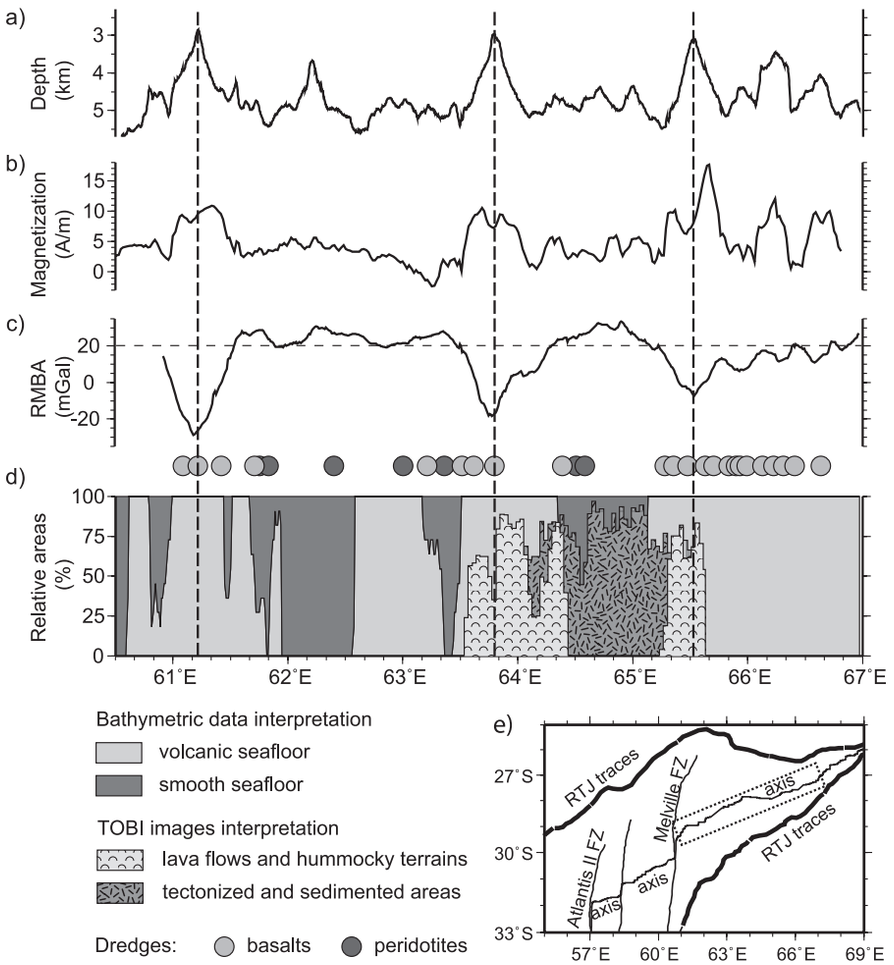

Figure 5. Along-axis variation of the magnetic, gravity, and bathymetric structures of the SWIR in the easternmost deep section of the SWIR between Melville TF and 67°E [after *Sauter et al.*, 2008]. Vertical dashed lines correspond to the centers of the high-relief ridge segments. (a) Along-axis variations in axial depth. (b) Along-axis variations in magnetization calculated by a 3-D inversion of the magnetic anomaly map with a constant-thickness source layer of 0.5 km whose upper surface is defined by the bathymetry (see *Sauter et al.* [2008] for further details). (c) Along-axis variations of the residual mantle Bouguer gravity anomalies (RMBA) from *Cannat et al.* [2006]. RMBA values were calculated from ship free-air gravity by subtracting first the effect of topography and of a constant density, constant thickness crust (3.4 km; the mean seismic crustal thickness determined near 66°E) [*Muller et al.*, 1999], then the effect of upper mantle cooling with age. (d) Along-axis distribution (in percent of mapped area in the 7-nm-wide strip along the axis) of the smooth nonvolcanic morphology and volcanic seafloor textures, as observed on the bathymetric map [*Cannat et al.*, 2006] and of the tectonized and volcanic areas observed on TOBI images [*Sauter et al.*, 2004b]. The fit is good between these two distributions; TOBI-derived morphological analysis having a greater resolution. Dots above Figure 5d show the dominant lithologies observed during five manned submersible dives of the Shinkai 6500 during the "Indoyo" cruise [*Fujimoto et al.*, 1999] and found in dredges performed during the "Edul" cruise [*Mével et al.*, 1997; *Meyzen et al.*, 2003], the "Discovery 208" cruise [*Robinson et al.*, 2001], the "Atlantis II 093-5" cruise [*Price et al.*, 1986], and the "Antipode" cruise [*Mahoney et al.*, 1989]. (e) Location map. The dotted frame indicates the portion of the SWIR axis shown in Figure 5.

There are no seismic data along such deep nonvolcanic sections along the SWIR, but the variations of seismic velocities in similar areas of the ultraslow spreading Gakkel ridge are related to a nonuniform thickness or even an absence of basalts with virtually no seismic layer 3 [*Jokat et al.*, 2003; *Jokat and Schmidt-Aursch*, 2007]. High axial magnetization values (10–20 A m^{-1}) are only observed on top of the volcanic centers and not at segment ends along the present-day axis [*Dick et al.*, 2003; *Hosford et al.*, 2003; *Sauter et al.*, 2004a] (Figure 5), contrary to what has been observed in many segments of the MAR [e.g., *Ravilly et al.*, 1998]. Rather, weak magnetizations (~5 A m^{-1}) are observed in both volcanic areas at segment ends and in the nonvolcanic deep sections of the ridge [*Dick et al.*, 2003; *Sauter et al.*, 2004b]. Variations of the thickness and the intrinsic magnetization of the basaltic source layer (with age and increasing low-temperature oxidative alteration) is probably dominating this along-axis magnetic signal [*Sauter et al.*, 2004b, 2008].

The large volcanic centers to the east of the Melville TF and in the oblique supersegment correspond to much higher along-axis slopes (up to 90 m km^{-1}) and have greater spacing (100–200 km) than the segment centers of the MAR (20–40 m km^{-1} and 50–60 km, respectively) [*Cannat et al.*, 1999; *Mendel et al.*, 1997]. They are associated with large-gravity low bull's eyes (Figure 5) indicating thick crust (up to 6 km in the segment centers) [*Cannat et al.*, 2003; *Dick et al.*, 2003; *Rommevaux-Jestin et al.*, 1997; *Standish et al.*, 2008]. By contrast, the deep and long ridge sections between the volcanic centers correspond to strong positive gravity anomalies indicating much thinner crust [*Cannat et al.*, 2003; *Dick et al.*, 2003] (Figure 5). The along-axis variation of the gravity-derived crustal thickness, tied to seismic data [*Minshull et al.*, 2006; *Muller et al.*, 1999] reveals that while each MAR segment is supplied with close to the regional average amount of melt [e.g., *Hooft et al.*, 2000], the volcanic segments in the easternmost part of the SWIR receive more melt than the regional average (e.g., ~4.7 km on average seismic crustal thickness for the volcanic segment located at 65°30′E versus ~3.7 km on average for the 100 km section in the 66°E area) [*Cannat et al.*, 2003]. It is difficult to give a precise estimation of the crustal thickness in the deep nonvolcanic areas, as seismic data are lacking there and the crust modeled from gravity uses the constant crustal density assumption, which is probably invalid because of significant lateral density variations within the crust, particularly where partially serpentinized mantle-derived rocks are exposed in the seafloor (see *Cannat et al.* [2006] and *Cannat et al.* [2008a] for a detailed discussion of the effect of serpentinized peridotites in the crust).

The ridge axis in the large volcanic centers of the eastern SWIR and of the oblique supersegment (9–15°E) is subperpendicular to the spreading direction, whereas the orientation of the deep nonvolcanic sections is highly variable. The volcanic centers in the oblique supersegment (the Joseph Mayes Seamount and the Narrowgate segment) limit three nonvolcanic sections with a 51° obliquity [*Dick et al.*, 2003; *Standish et al.*, 2008]. The nonvolcanic sections in the easternmost SWIR are nearly orthogonal to spreading (between 64° and 66°E) or have an intermediate obliquity (33° from the Melville TF to a change in ridge trend at ~64°E) [*Cannat et al.*, 2006]. These two neighboring nonvolcanic sections of the ridge thus have contrasting obliquities (33° and 5°), yet they show only a slight (0.5 km) difference in the regional gravity-derived crustal thickness [*Cannat et al.*, 2008a]. Ridge obliquity is expected to have an effect on melt production [e.g., *Montési and Behn*, 2007]. As a ridge becomes oblique to the spreading direction, its length increases per unit of lithosphere created, and mantle upwelling must slow proportionally to conserve mass [*Dick et al.*, 1998]. *Cannat et al.* [2008a] proposed that this effect is significant (about 1.5 km less melt produced for a decrease of 7 to 4 mm a^{-1} in effective spreading rates for a ridge section with an obliquity of 50°) but not enough to produce near-amagmatic spreading in the most oblique regions of the ridge, unless associated with an anomalously cold and/or depleted mantle source.

It has been argued that the oblique region of the SWIR between the Gallieni and Atlantis II TFs (with a 30° obliquity) also comprises "amagmatic" sections [*Baines et al.*, 2007; *Dick et al.*, 2003]. These oblique sections of the ridge were first described as oblique nontransform discontinuities [*Sauter et al.*, 2001]. They present some similarities with the nonvolcanic ridge sections found in the oblique supersegment or in the easternmost SWIR. They are longer than the neighboring segments and present positive MBAs and a weak magnetization [*Mendel et al.*, 2003; *Sauter et al.*, 2004a]. However, these oblique sections of the ridge also display seafloor morphologies quite distinct from those in the nonvolcanic areas described further east. Occasional volcanic cones and patterns of NE and EW trending scarps suggest complex interplays between spreading-perpendicular extension and transform tectonics [*Cannat et al.*, 2008a]. Moreover, a few dredges in these areas recovered mainly serpentinized peridotites but also abundant basalts, dolerites, and massive gabbros [*Seyler et al.*, 2003]. Forward modeling showed that the amplitude of the central magnetic anomaly was best estimated with models using a basaltic source layer thickness decreasing from 500 m on top of the segments up to 100 m in the deepest part of the discontinuities [*Sauter et al.*, 2004a]. Side-scan sonar exploration also documented many small spreading-perpendicular volcanic ridges in the oblique ridge section between the Novara and Melville TFs (with a ~30° obliquity) [*Sauter et al.*, 2002]. Volcanism is

thus highly variable along the oblique sections of the SWIR and some nonvolcanic segments are orthogonal to the spreading direction, as on the Gakkel ridge [*Dick et al.*, 2003]. This shows that the formation of nonvolcanic ridge sections is not determined only by ridge obliquity.

6. A 26-MYR-LONG RECORD OF AXIAL TECTONIC AND MAGMATIC PROCESSES IN THE EASTERNMOST MELT POOR SECTION OF THE SWIR

Bathymetry, gravity, and magnetic data collected in the eastern SWIR (between 61° and 67°E), over a 660-km-long section and for crustal ages up to 26 Ma, are the most extensive available for an ultraslow ridge and provide the first opportunity to study the time and space evolution of spreading processes in this end-member spreading context [*Cannat et al.*, 2006]. Magnetic anomalies show that the plate boundary geometry in this area has been stable over at least the past 26 Myr. However, between 63°15′ and 64°30′E, the ridge flanks do not display clear traces of past axial segmentation. The off-axis gravity low bull's eyes, indicating short (<3 Myr) melt supply events, appear heterogeneously distributed and occur mostly in the African plate after magnetic anomaly C6. Off-axis crustal thickness, as modeled from gravity anomalies, is on average larger in the northern than in the southern ridge flank, suggesting persistent tectonic asymmetry [*Cannat et al.*, 2006; *Searle and Bralee*, 2007]. This pattern has no equivalent in other sets of mid-ocean gravity data.

This survey area displays the widest expanses known to date of seafloor with no evidence for a volcanic upper crustal layer (~37% of the axial and off-axis seafloor generated in this survey area) [*Cannat et al.*, 2006]. This nonvolcanic ocean floor has no equivalent at faster spreading ridges and has been called "smooth seafloor" because it occurs in the form of broad ridges, with a smooth, rounded topography [*Cannat et al.*, 2006] (Figure 6). It shows no resolvable volcanic cones on bathymetric data [*Cannat et al.*, 2006]. The absence of volcanic edifices is confirmed by available deep-tow sonar data [*Sauter et al.*, 2004b; *Searle et al.*, 1999; *Searle and Bralee*, 2007] and the abundance of serpentinized mantle-derived peridotites, with minor basalts and gabbros dredged in the axial valley [*Seyler et al.*, 2003] (see above and Figure 5). Seafloor with unambiguous volcanic features represents ~59% of the mapped area. Corrugated surfaces, similar to those described at faster ridges [*Searle et al.*, 1999] and interpreted as exhumed detachment fault surfaces [*Cann et al.*, 1997; *Tucholke et al.*, 1998], represent 4% of the mapped area. Volcanic seafloor is most commonly accreted to both plates (this configuration accounts for 40% of the seafloor). It is less commonly accreted on one plate with corrugated or smooth seafloor forming in conjugate crust.

Off-axis, the amplitudes of the magnetic anomalies are, on average, higher over volcanic seafloor areas, where thicker crust is inferred [low residual mantle Bouguer gravity anomalies (RMBA) values] and lower over smooth nonvolcanic seafloor with inferred thinner crust (high RMBA values) [*Sauter et al.*, 2008]. Local standard deviation of the magnetization, a proxy for magnetization contrast, is on average higher for volcanic seafloor than for smooth nonvolcanic topography suggesting that the contribution of the basaltic upper crustal layer to the production of magnetic anomalies remains important in off-axis regions (Figure 7). However, magnetic anomalies that record past magnetic polarity events are found almost everywhere in the survey area, even over domains that lack a volcanic upper crustal layer, arguing thus for the contribution of other sources like gabbros and/or serpentinized peridotites [*Sauter et al.*, 2008; *Searle and Bralee*, 2007]. Although not systematic, and weak over most parts of the survey area, an induced component of magnetization is clearly present in some nonvolcanic seafloor domains [*Sauter et al.*, 2008]. Serpentinized peridotites are the likely carriers of this induced magnetization component.

Smooth seafloor and most corrugated terrains correspond to high RMBA values (Figures 6–7). This is consistent with a lower magma input, all the more for the smooth seafloor terrain, because part of the crust there is made of exhumed mantle-derived peridotites. Corrugated surfaces also occur in areas of moderate RMBA (Figures 6–7), from which it has been inferred that they also form when the ridge magma supply is somewhat higher [*Cannat et al.*, 2006]. Volcanic terrains extend out of the RMBA low bull's eyes, corresponding to past large volcanic centers, into areas of higher RMBA values. This suggests that these higher RMBA volcanic areas form by lateral propagation of dikes away from the bull's eyes volcanic centers [*Cannat et al.*, 2006]. The volcanic centers in the 64°–66°E orthogonal ridge section are surrounded by wider expanses of volcanic terrains, while the oblique region from Melville TF to 64°E displays a larger proportion of nonvolcanic or nearly nonvolcanic smooth terrains suggesting that spreading obliquity leads to more focused volcanism [*Cannat et al.*, 2006].

Successive large-offset normal faults are inferred to develop preferentially in one ridge flank, producing a long-lasting asymmetry of crustal thickness and gravity signature between the two plates (Figure 8a) [*Cannat et al.*, 2006]. Successive principal axial faults can also face alternatively north and south, producing an overall symmetrical crustal thickness (and gravity) pattern. Corrugated seafloor in Figure 8b is inferred to form in the footwall of a detachment fault, with dikes and lava in the conjugate, hanging wall plate. This configuration accounts for only 7% of the seafloor accreted in the study area. The corrugated surface mode thus

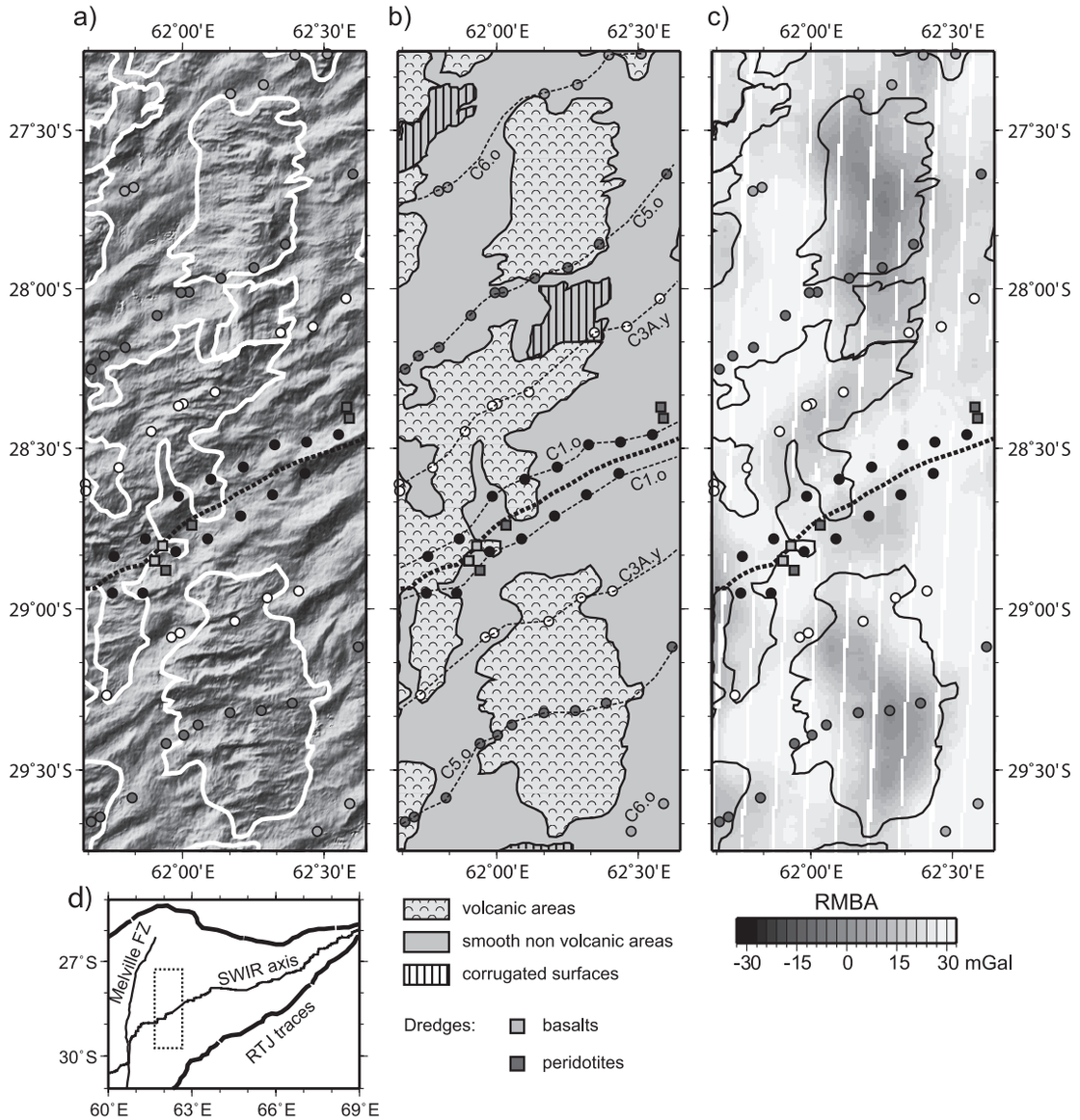

Figure 6. Off-axis bathymetry and gravity data showing volcanic and smooth nonvolcanic areas between 61°40′ and 62°40′E: (a) seafloor slope illuminated from 45°W, (b) map of seafloor morphologies, and (c) RMBA map after *Cannat et al.* [2006]. Three different types of seafloor morphologies were identified: corrugated surfaces, volcanic seafloor (displaying unambiguous volcanic features such as volcanic cones), and smooth seafloor occurring in the form of broad ridges, with a smooth, rounded topography and no resolvable volcanic cone. Note that tectonic ridges in smooth nonvolcanic areas are oblique to the spreading direction, while the smaller-scale tectonic features in the volcanic areas are orthogonal to the spreading direction. The 14-Myr-long interval between magnetic anomalies C6 and C3A corresponds to the formation of an elongated gravity low at ~62°E and to the emplacement of volcanic seafloor, reflecting enhanced melt supply for this period of time. Isochrons are drawn following the identification of magnetic anomalies of *Cannat et al.* [2006] using the geomagnetic reversal time scale of *Cande and Kent* [1995]: C1.o (Brunhes/Matuyama 0.780 Ma); C3A.y (5.894 Ma), C5.o (10.949 Ma), C6.o (20.131 Ma) (y and o stand for the young and old edge of the magnetic block, respectively). The thick dashed black line indicates the axis. (d) Location map. The dotted frame indicates the portion of the SWIR axis shown in this image.

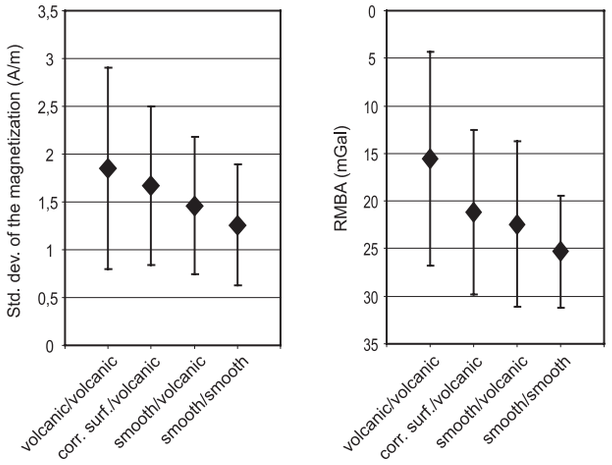

Figure 7. Comparison between seafloor morphology, standard deviation of the magnetization, and gravity signature using the grid of conjugate domains of *Cannat et al.* [2006] [after *Sauter et al.*, 2008]. Four types of conjugate pairs (volcanic-volcanic, corrugated-volcanic, smooth-volcanic, and smooth-smooth) inferred to have formed simultaneously on each side of the axial valley are plotted in order of decreasing standard deviation of the magnetization (or decreasing magnetic contrast) and increasing mean RMBA (or decreasing mean crustal thickness). Conjugate volcanic seafloor systematically has higher magnetization contrast and lower mean RMBA (or thicker crust), while conjugate smooth seafloor systematically has lower magnetization contrast and higher mean RMBA (or thinner crust).

appears to correspond to a narrow window of magmatic and/or tectonic conditions, as proposed on the basis of numerical models of axial faulting [*Buck et al.*, 2005; *Tucholke et al.*, 2008]. Some corrugated surfaces have a large extension along axis, others are very narrow. Such narrow surfaces likely represent the exposed portion of wider detachment faults buried beneath entrained blocks of hanging wall volcanics [*Smith et al.*, 2006, 2008]. Smooth seafloor is either accreted to both plates (23% of total mapped area) or faces volcanic seafloor in conjugate crust (28% of total mapped area). Smooth seafloor probably forms by frequent shifts in the polarity of axial valley-bounding normal faults and shear zones, leading to fault capture, and to an essentially symmetrical overall tectonic pattern (Figure 8c) [*Cannat et al.*, 1997]. The ridge-parallel trend of the observed horst and graben morphology, even in oblique spreading regions, suggests that failure is localized by the axis of lithospheric necking at the base of the plate [*Dick et al.*, 2003]. Smooth seafloor occasionally bears faint corrugations, suggesting that, in favorable conditions (e.g., higher melt supply), axial valley bounding faults evolve into corrugated detachments (Figures 8b and 8c).

7. MECHANISMS FOR ALONG-AXIS MELT FOCUSING AND REDISTRIBUTION

The large volcanic centers in the easternmost and westernmost parts of the SWIR are substantially shorter-lived than most segments of the MAR and have much higher relief-to-length ratios than along the MAR [*Cannat et al.*, 1999; *Mendel et al.*, 1997; *Standish et al.*, 2008]. Those to the east

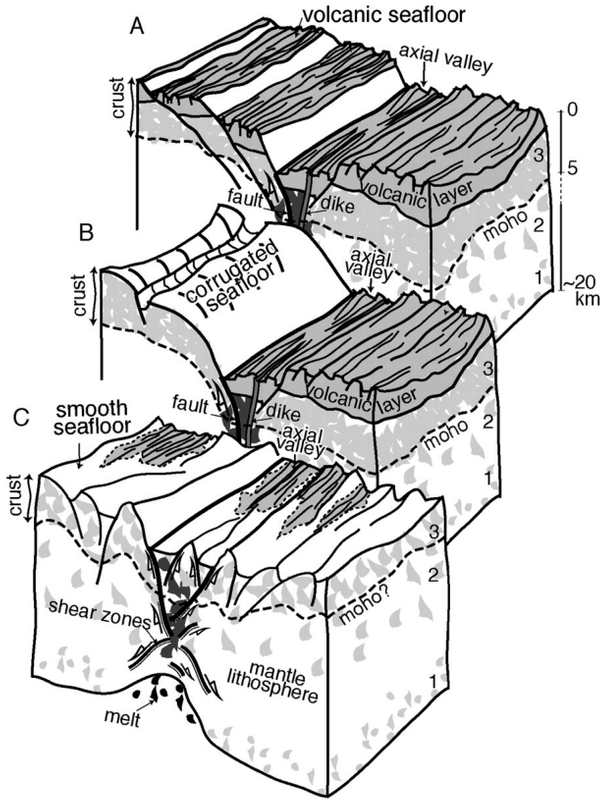

Figure 8. Lithosphere-scale sketches of axial region for three proposed modes of melt-poor ultraslow spreading, shown in order of inferred decreasing melt supply [after *Cannat et al.*, 2006]. Modes A (volcanic-volcanic) and B (corrugated-volcanic) also develop at faster spreading Mid-Atlantic Ridge and in more magmatically robust regions of ultraslow ridges. Mode C (smooth-smooth or smooth-volcanic), with little to no axial volcanism, appears specific to melt-poor ultraslow ridges. Horizontal dimensions are ~80 km across axis, and ~40 km along axis. Melt concentrations are shown in black (in asthenosphere), or dark gray (in lithosphere). Crystallized magmatic rocks are shown in lighter shade of gray. Abundance of magmatic rocks at different levels of crust and mantle lithosphere (1, 2, and 3) is expected to vary as a function both of how much melt crystallized at which depth and of how much of crystallized material was then tectonically transported to higher levels [*Cannat*, 1996].

of Melville TF receive more melt than the regional average, whereas each MAR segment is supplied with close to the regional average amount of melt [*Cannat et al.*, 2003]. Melt supply appears thus to be more focused along the easternmost part of the SWIR than at the MAR. The large along-axis variations in crustal thickness in the oblique supersegment may also be explained by along-axis focusing of melt [*Standish et al.*, 2008].

Melt focusing at the large volcanic centers of the SWIR could result from a combination of melt migration near the base of the lithosphere and rapid melt extraction through dikes rooted in melt-rich regions [*Cannat et al.*, 1999, 2003, 2008a]. Triggering along-axis melt migration requires a sloping horizon. This could result from a localized increase in melt supply caused by a diapiric instability in the mantle [*Lin et al.*, 1990] or by melting of a small domain of enriched mantle [*Bonatti*, 1990]. Most melts that reach the base of the lithosphere are likely to have been extracted from the melting mantle at some depth underneath and are therefore expected to be generally warmer than the surrounding mantle. The base of the lithosphere could therefore be thermally eroded wherever most melts have gathered. Once topography is created at the base of the lithosphere, melts will migrate along this sloping horizon [*Sparks and Parmentier*, 1991] and gather beneath what then becomes the center of a thick crust ridge segment. The zone of potential melt contribution is much greater than on the MAR, as the spacing between large volcanic centers is larger at the eastern and westernmost parts of the SWIR than on the MAR (Figure 9) [*Mendel et al.*, 1997; *Standish et al.*, 2008]. The building of the large SWIR volcanic centers requires also that a significant proportion of the magma, which gathers at the base of the lithosphere, has to be channeled through the axial lithosphere instead of forming sills or plutons at midcrustal to lower crustal levels. Dikes, rooting in the magma-rich regions at the base of the axial lithosphere (Figure 10), have been proposed as the dominant mode of melt transport [*Cannat et al.*, 1999; *Dick*, 1989].

Temperature is the main factor controlling rheology in the oceanic lithosphere, and melt advection is the most efficient way to provide heat to mid-ocean ridges [*Sleep*, 1975]. This setup could thus, in principle, be self maintained, melt migration toward the segment center providing the heat required to keep the lithosphere thin at this location. Variation of the local melt supply to the ridge would produce modifications in the melt distribution process. Magnetic and seafloor

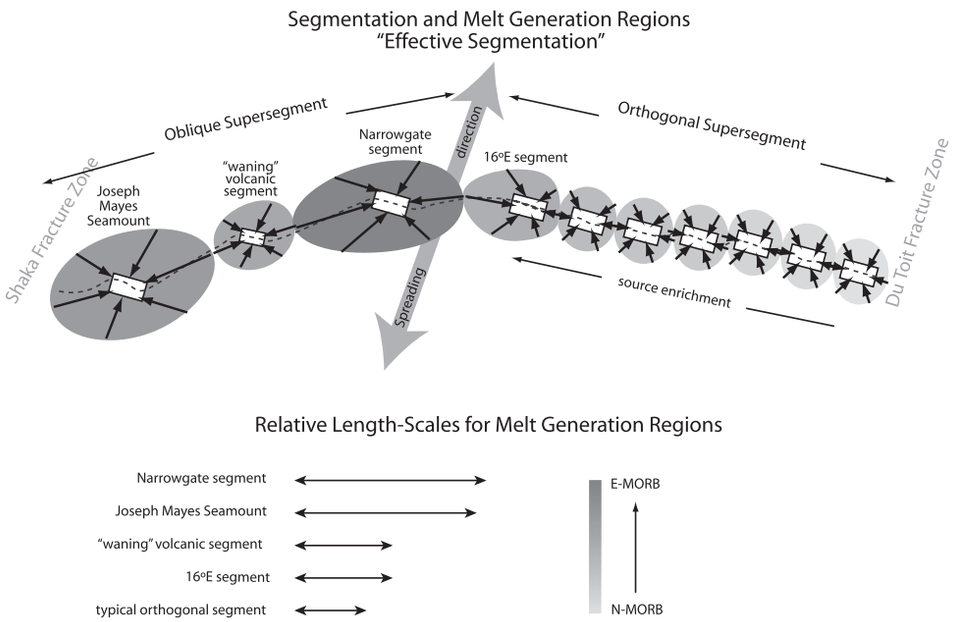

Figure 9. Schematic illustration (map view) of 9°–25°E magmatic segmentation and associated "effective segmentation" [after *Standish et al.*, 2008]. Small black arrows indicate simplified direction of melt focusing beneath each magmatic segment, based on modeled flow lines [*Montési and Behn*, 2007] and theoretical slope of lithospheric base. Variably shaded gray ovals represent the "effective segmentation" for each magmatic segment derived from segment spacing and along-axis lithospheric topography. The shade of gray reflects the relative enrichment of lavas for each segment and is a function of the mantle source, but more so the "effective segmentation." Dashed line is the ridge axis.

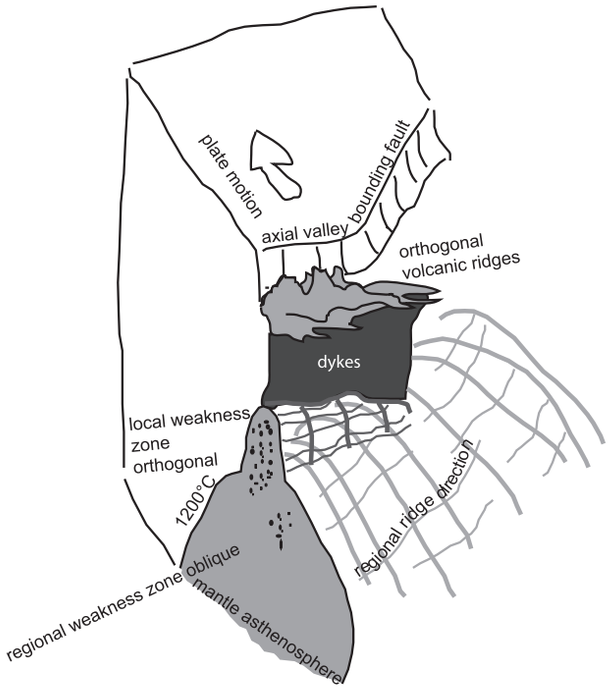

Figure 10. Sketch of an oblique spreading ultraslow ridge [after *Cannat et al.*, 2008a]. Only one lithospheric plate is shown in order to view the lithosphere-asthenosphere boundary (assumed to lie close to the 1200°C isotherm). Owing to mantle upflow and melt migration, this boundary shallows in the axial region, forming a zone of weakness that guides axial valley bounding faults. This regional zone of weakness (or asthenospheric channel) has an oblique trend at scales greater than 100 km. Repeated dike injections should feed orthogonal volcanic ridges in areas of high melt supply. These injections heat the mantle lithosphere, forming local and shallower weakness zones, also orthogonal to spreading. Axial valley bounding faults reorient, following these local weakness zones. The typical dimension for orthogonal sections in oblique regions of the SWIR is 40 to 50 km. Dike propagation in these oblique ridge regions should be limited by the width of the regional lithospheric weakness zone in the direction orthogonal to spreading.

morphology off-axis data for the present-day nonvolcanic oblique segment at 62°E, suggest that the faults that bound oblique sections of the axial valley reoriented to spreading perpendicular within 1 or 2 Ma [*Cannat et al.*, 2008a] (Figure 6). Gravity data show that this reorientation takes place during episodes of enhanced melt supply [*Cannat et al.*, 2008a] (Figure 6). The mechanism proposed for this local reorientation of the ridge following an enhanced melt supply event is that large volumes of melt are transported through the lithospheric mantle and through the crust in dikes that form perpendicular to the direction of least compressive stress (Figure 10). This creates a hot orthogonal zone of weakness in the axial lithosphere and promotes the formation of orthogonal axial valley bounding faults [*Cannat et al.*, 2008a]. The length of the resulting orthogonal ridge region is limited by the length of dike swarms feeding eruptions at the seafloor. When melt supply decreases, the disruption of the volcanic edifices by faults that reach deep into the axial lithosphere and channel hydrothermal fluids may be the cause of a rapid cooling of the lithosphere [*Cannat et al.*, 2003]. Variations in local melt transport, small-scale mantle heterogeneities, and prior mantle melting history can also result in large local variations in the extent of mantle-melt reaction and MORB chemistry [*Standish et al.*, 2008].

Nonvolcanic or nearly nonvolcanic sections of the ridge represent the most distal parts of the crustal melt distribution system, out of the reach of most dikes that root in centers of enhanced melt supply (Figure 10). The resulting segmentation pattern, with prominent volcanic centers and long intervening melt-poor ridge sections, is not specific to oblique ridge regions (see above). Sections of the ridge that do receive some melt, but not enough to build sufficient magmatic overpressure and open a dike conduit through the thick axial lithosphere, are more likely to develop a crustal architecture with trapped melt in the lithospheric mantle. This may be the case beneath the long nonvolcanic sections of the ridge east of Melville TF and also beneath the long oblique supersegment in the westernmost part of the SWIR [*Cannat et al.*, 2008a; *Standish et al.*, 2008]. In these two sections of the ridge, the axial lithosphere is presumably thick enough to support large volcanic centers and to impede dike formation unless large volumes of melt can gather and build sufficient overpressure.

8. OUTSTANDING QUESTIONS

What we have learned about the SWIR over the past two decades leads to more questions and to hypothesis which should now be tested. Are nonvolcanic sections of the ridge nearly amagmatic, or is melt trapped in the deep mantle lithosphere? How does the structure of the crust vary between the volcanic centers and the neighboring nonvolcanic sections? Does the magma pool in a deep reservoir near the base of the ductile lithosphere, and is there a shallower magma chamber beneath the large volcanic centers? How is the magma channeled through the crust at and near these volcanic centers? Seismic data are sorely missing in both the large volcanic centers and in the exhumed mantle domains of the SWIR. They would provide precious constraints to address these questions.

There are also a number of issues that have not been properly addressed so far because of a lack of microseismicity studies. Is there a systematic change in the focal depth distribution of seismic events with distance to the large volcanic centers? What

are the mechanisms and the moment release of seismic events in the mantle-exhumation domains? A microearthquake survey could also give key diagnostic information on the rheology, the mechanical structure, and the thermal state of the lithosphere in the nonvolcanic sections of the SWIR axis.

What controls the peculiar segmentation of the deeper and melt-poor regions of the SWIR? The easternmost SWIR lacks a long-lasting segmentation pattern. It therefore may provide a unique opportunity to relate the surface distribution of volcanism and the along-axis variations in crustal thickness, to active processes, and to the distribution of heterogeneities in the upwelling asthenospheric mantle below the ridge. This is in contrast to the MAR setting, where along-axis variations in the mechanical and thermal structure of the lithosphere due to long-lasting axial discontinuities may also contribute to the 3-D geometry of the melt plumbing system. A tomographic experiment with passive arrays of seismometers and hydrophones deployed in the easternmost SWIR during a few months would help constrain the variation of seismic velocities and seismic anisotropy in the mantle along the ridge, the density structure, and the distribution of the melt content in the mantle between two large volcanic centers. These results would contribute significantly to our understanding of asthenospheric processes associated with magma generation, transport, and segmentation at mid-ocean ridges.

Acknowledgments. We are grateful to many colleagues, particularly to Philippe Patriat, Véronique Mendel, Céline Rommevaux-Jestin, Eric Humler, Eric Debayle, Antoine Bezos, Christine Meyzen, Cécile Gautheron, Heather Sloan, Marc Munschy, Armelle Bernard, Anne Briais, Kyoko Okino, Luc Lavier, Catherine Mével, Javier Escartin, Lindsay Parson, Bramley Murton, Roger Searle, Nancy Grindlay, Jeff Standish, and Henry Dick for discussions, which helped us through this work. We thank the captains, officers, and crews of the R/V *Marion Dufresne* from IPEV and R/V *L'Atalante* from IFREMER for their assistance during several French and InterRidge cruises at the SWIR. The FUJI cruise was co-funded by Japan and France, and the TOBI operations were supported by the European Community through an EASSS program. Participation in the cruise and postcruise studies was supported by the French Centre National de la Recherche Scientifique (CNRS-INSU). We thank Nancy Grindlay and Jeff Standish who gave us access to some of their data. We also thank one anonymous reviewer, Henry Dick, and Bramley Murton for constructive reviews and suggestions. We have used the PetDB data set [*Lehnert et al.*, 2000] to find the composition of rocks dredged along the SWIR. Figures were created using the public domain GMT software [*Wessel and Smith*, 1995]. We use the MODMAG software [*Mendel et al.*, 2005] to model marine magnetic anomalies. This is IPGP contribution 2502.

REFERENCES

Baines, A. G., M. J. Cheadle, H. J. B. Dick, A. H. Scheirer, B. E. John, N. J. Kusznir, and T. Matsumoto (2007), Evolution of the Southwest Indian Ridge from 55°45′E to 62°E: Changes in plate-boundary geometry since 26 Ma, *Geochem. Geophys. Geosyst.*, *8*(6), Q06022, doi:10.1029/2006GC001559.

Ben-Avraham, Z., C. J. H. Hartnady, and A. P. L. Roex (1995), Neotectonic activity on continental fragments in the Southwest Indian Ocean: Agulhas au and Mozambique Ridge, *J. Geophys. Res.*, *100*(B4), 6199–6211.

Bergh, H. W., and D. M. Barrett (1980), Aghulas Basin magnetic bight, *Nature*, *287*, 591–595).

Bernard, A., M. Munschy, Y. Rotstein, and D. Sauter (2005), Refined spreading history at the Southwest Indian Ridge for the last 96 Ma, with the aid of satellite gravity data, *Geophys. J. Int.*, *162*(3), 765–778.

Bonatti, E. (1990), Not so hot "hot spots" in the oceanic mantle, *Science*, *250*, 107–111.

Bown, J. W., and R. S. White (1994), Variation with spreading rate of oceanic crustal thickness and geochemistry, *Earth Planet. Sci. Lett.*, *121*, 435–449.

Brunelli, D., A. Cipriani, L. Ottolini, A. Peyve, and E. Bonatti (2003), Mantle peridotites from the Bouvet Triple Junction Region, South Atlantic, *Terra Nova*, *15*, 194–203, doi: 110.1046/j.1365-3121.2003.00482.x.

Buck, W. R., L. L. Lavier, and A. N. B. Poliakov (2005), Modes of faulting at mid-ocean ridges, *Nature*, *434*, 719–723.

Cande, S. C., and D. V. Kent (1995), Revised calibration of the geomagnetic polarity timescale for the Late Cretaceous and Cenozoic, *J. Geophys. Res.*, *100*(B4), 6093–6095.

Cann, J. R., D. K. Blackman, D. K. Smith, E. McAllister, B. Janssen, S. Mello, E. Avgerinos, A. R. Pascoe, and J. Escartín (1997), Corrugated slip surfaces formed at North Atlantic ridge-transform intersections, *Nature*, *385*, 329–332.

Cannat, M. (1996), How thick is the magmatic crust at slow spreading oceanic ridges?, *J. Geophys. Res.*, *101*(B2), 2847–2857.

Cannat, M., Y. Lagabrielle, H. Bougault, J. Casey, N. de Coutures, L. Dmitriev, and Y. Fouquet (1997), Ultramafic and gabbroic exposures at the Mid-Atlantic Ridge: Geological mapping in the 15°N region, *Tectonophysics*, *279*, 193–213.

Cannat, M., C. Rommevaux-Jestin, D. Sauter, C. Deplus, and V. Mendel (1999), Formation of the axial relief at the very slow spreading Southwest Indian Ridge (49°–69°E), *J. Geophys. Res.*, *104*(B10), 22,825–22,843.

Cannat, M., C. Rommevaux-Jestin, and H. Fujimoto (2003), Melt supply variations to a magma-poor ultra-slow spreading ridge (Southwest Indian Ridge 61° to 69°E), *Geochem. Geophys. Geosyst.*, *4*(8), 9104, doi:10.1029/2002GC000480.

Cannat, M., J. Cann, and J. Maclennan (2004), Some hard rock constraints on the supply of heat to mid-ocean ridges, in *The Thermal Structure of the Ocean Crust and Dynamics of Hydrothermal Circulation*, edited by C. German et al., pp. 111–149, AGU, Washington, D. C.

Cannat, M., D. Sauter, V. Mendel, E. Ruellan, K. Okino, J. Escartin, V. Combier, and M. Baala (2006), Modes of seafloor generation at a melt-poor ultraslow-spreading ridge, *Geology*, *34*(7), 605–608.

Cannat, M., D. Sauter, A. Bezos, C. Meyzen, E. Humler, and M. Le Rigoleur (2008a), Spreading rate, spreading obliquity,

and melt supply at the ultraslow spreading Southwest Indian Ridge, *Geochem. Geophys. Geosyst.*, *9*, Q04002, doi:10.1029/2007GC001676.

Cannat, M., D. Sauter, L. Lavier, and J. Escartin (2008b), Oceanic corrugated surfaces and the strength of the axial lithosphere at slow spreading ridges, *Eos Trans. AGU*, *89*(53), Fall Meet. Suppl., Abstract T34A-01.

Cannat, M., D. Sauter, J. Escartín, L. Lavier, and S. Picazo (2009), Oceanic corrugated surfaces and the strength of the axial lithosphere at slow spreading ridges, *Earth Planet. Sci. Lett.*, *288*, 174–183.

Chu, D., and R. G. Gordon (1999), Evidence for motion between Nubia and Somalia along the Southwest Indian Ridge, *Nature*, *398*, 64–67.

Debayle, E., and J. J. Lévêque (1997), Upper mantle heterogeneities in the Indian Ocean from waveform inversions, *Geophys. Res. Lett.*, *24*(3), 245–248.

Debayle, E., B. Kennett, and K. Priestley (2005), Global azimuthal seismic anisotropy and the unique plate-motion deformation of Australia, *Nature*, *433*, 509–512.

Dick, H. J. B. (1989), Abyssal peridotites, very slow spreading ridges and ocean ridge magmatism, in *Magmatism in the Ocean Basins*, *Geol. Soc. Spec. Publ.*, vol. 42, edited by A. D. Saunders and M. J. Norry, pp. 71–105.

Dick, H. J. B., H. Schouten, P. S. Meyer, D. G. Gallo, H. Bergh, R. Tyce, P. Patriat, K. T. M. Johnson, J. Snow, and A. Fischer (1991), Tectonic evolution of the Atlantis II Fracture Zone, in *Proc. Ocean Drill. Program Sci. Results*, vol. 118, edited by R. P. Von Herzeen et al., pp. 359–398, Ocean Drill. Program, College Station, TX.

Dick, H. J. B., P. T. Robinson, and P. S. Meyer (1992), The plutonic foundation of a slow-spreading ridge, in *Synthesis of Results from Scientific Drilling in the Indian Ocean*, *Geophys. Monogr. Ser.*, vol. 70, edited by R. A. Duncan et al., pp. 1–39, AGU, Washington, D. C.

Dick, H. J. B., J. E. Georgen, A. P. L. Roex, J. Lin, and J. A. Madsen (1998), The influence of ridge geometry on mantle melting at an ultra-slow spreading ridge, *Eos Trans. AGU*, *79*, Fall Meet. Suppl., Abstract F919.

Dick, H. J. B., et al. (2000), A long in situ section of the lower oceanic crust: Results of ODP leg 176 drilling at the Southwest Indian Ridge, *Earth Planet. Sci. Lett.*, *179*, 31–51.

Dick, H. J. B., J. Lin, and H. Schouten (2003), An ultraslow-spreading class of ocean ridge, *Nature*, *426*, 405–412.

Dyment, J. (1993), Evolution of the Indian Ocean triple junction between 65 and 49 Ma (Anomalies 28 to 21), *J. Geophys. Res.*, *98*(B8), 13,863–13,877.

Dziewonski, A. M., and D. L. Anderson (1981), Preliminary reference earth model, *Phys. Earth Planet. Inter.*, *25*(4), 297–356.

Eagles, G., and M. Konig (2008), A model of plate kinematics in Gondwana breakup, *Geophys. J. Int.*, *137*(2), 703–717.

Escartín, J., and M. Cannat (1999), Ultramafic exposures and the gravity signature of the lithosphere near the Fifteen-Twenty Fracture Zone (Mid-Atlantic Ridge, 14°–16.5°N), *Earth Planet. Sci. Lett.*, *171*, 411–424.

Fisher, R. L., and A. M. Goodwillie (1997), The physiography of the Southwest Indian Ridge, *Mar. Geophys. Res.*, *19*, 451–455.

Font, L., B. J. Murton, S. Roberts, and A. G. Tindle (2007), Variations in melt productivity and melting conditions along SWIR (70°E-49°E): Evidence from olivine-hosted and plagioclase-hosted melt inclusions, *J. Petrol.*, *48*(8), 1471–1494.

Fujimoto, H., et al. (1999), First submersible investigations of mid-ocean ridges in the Indian Ocean, *InterRidge News*, *8*, 22–24.

Georgen, J. E. (2008), Mantle flow and melting beneath oceanic ridge-ridge-ridge triple junctions, *Earth Planet. Sci. Lett.*, *270*, 231–240.

Georgen, J. E., and J. Lin (2002), Three-dimensional passive flow and temperature structure beneath ridge-ridge-ridge triple junctions, *Earth Planet. Sci. Lett.*, *204*, 115–132.

Georgen, J. E., J. Lin, and H. J. B. Dick (2001), Evidence from gravity anomalies for interactions of the Marion and Bouvet hotspots with the Southwest Indian Ridge: Effects of transform offsets, *Earth Planet. Sci. Lett.*, *187*, 283–300.

Gomez, O., A. Briais, D. Sauter, and V. Mendel (2006), Tectonics at the axis of the very slow spreading Southwest Indian Ridge: Insights from TOBI side-scan sonar imagery, *Geochem. Geophys. Geosyst.*, *7*(5), Q05K12, doi:10.1029/2005GC000955.

Gràcia, E., J. L. Charlou, J. R. Radford-Knoery, and L. M. Parson (2000), Non-transform offsets along the Mid-Atlantic Ridge south of the Azores (38°N–34°N): Ultramafic exposures and hosting of hydrothermal vents, *Earth Planet. Sci. Lett.*, *177*, 89–103.

Grindlay, N. R., J. A. Madsen, C. Rommevaux, and J. Sclater (1998), A different pattern of ridge segmentation and mantle Bouguer gravity anomalies along the ultra-slow spreading Southwest Indian Ridge (15°30′E to 25°E), *Earth Planet. Sci. Lett.*, *161*, 243–253.

Honsho, C., K. Tamaki, and H. Fujimoto (1996), Three-dimensional magnetic and gravity studies of the Rodriguez Triple Junction in the Indian Ocean, *J. Geophys. Res.*, *101*(B7), 15,837–15,848.

Hooft, E. E. E., R. S. Detrick, D. R. Toomey, J. A. Collins, and J. Lin (2000), Crustal thickness and structure along three contrasting spreading segments of the Mid-Atlantic Ridge, 33.5°–35°N, *J. Geophys. Res.*, *105*(B4), 8205–8226.

Horner-Johnson, B. C., R. G. Gordon, S. M. Cowles, and D. F. Argus (2005), The angular velocity of Nubia relative to Somalia and the location of the Nubia–Somalia–Antarctica triple junction, *Geophys. J. Int.*, *162*(1), 221–238.

Horner-Johnson, B. C., R. G. Gordon, and D. F. Argus (2007), Plate kinematic evidence for the existence of a distinct plate between the Nubian and Somalian plates along the Southwest Indian Ridge, *J. Geophys. Res.*, *112*, B05418, doi:10.1029/2006JB004519.

Hosford, A., M. Tivey, T. Matsumoto, H. Dick, H. Schouten, and H. Kinoshita (2003), Crustal magnetization and accretion at the Southwest Indian Ridge near the Atlantis II fracture zone, 0–25 Ma, *J. Geophys. Res.*, *108*(B3), 2169, doi:10.1029/2001JB000604.

Janney, P. E., A. P. L. Roex, and R. W. Carlson (2005), Hafnium isotope and trace element constraints on the nature of mantle heterogeneity beneath the Central Southwest Indian Ridge (13°E to 47°E), *J. Petrol.*, *46*(12), 2427–2464.

Jokat, W., and M. C. Schmidt-Aursch (2007), Geophysical characteristics of the ultraslow spreading Gakkel Ridge, Arctic Ocean, *Geophys. J. Int.*, *168*(3), 983–998.

Jokat, W., O. Ritzmann, M. C. Schmidt-Aursch, S. Drachev, S. Gauger, and J. Snow (2003), Geophysical evidence for reduced melt production on the Arctic ultraslow Gakkel mid-ocean ridge, *Nature*, *423*(26), 962–965.

Klein, E. M., and C. H. Langmuir (1987), Global correlations of ocean ridge basalt chemistry with axial depth and crustal chemistry, *J. Geophys. Res.*, *92*(B8), 8089–8115.

Kuhn, T., D. Burger, D. Castradori, and P. Halbach (2000), Volcanic and hydrothermal history of ridge segments near the Rodrigues Triple Junction (Central Indian Ocean) deduced from sediment geochemistry, *Mar. Geol.*, *169*(3–4), 391–409.

Langmuir, C. H., E. M. Klein, and T. Plank (1992), Petrological systematics of mid-ocean ridge basalts: Constraints on melt generation beneath mid-ocean ridges, in *Mantle Flow and Melt Generation at Mid-Ocean Ridges*, edited by J. Phipps Morgan et al., pp. 183–280, AGU, Washington, D. C.

Lehnert, K., Y. Su, C. H. Langmuir, B. Sarbas, and U. Nohl (2000), A global geochemical database structure for rocks, *Geochem. Geophys. Geosyst.*, *1*(5), 1012, doi:10.1029/1999GC000026.

Lemaux, J., R. G. Gordon, and J. Y. Royer (2002), Location of the Nubia-Somalia boundary along the Southwest Indian Ridge, *Geology*, *30*(4), 339-342.

LeRoex, A. P., H. J. B. Dick, A. J. Erlank, A. M. Reid, F. A. Frey, and S. R. Hart (1983), Geochemistry, mineralogy and petrogenesis of lavas erupted along the Southwest Indian Ridge between the Bouvet Triple Junction and 11°E, *J. Petrol.*, *24*, 267–318.

LeRoex, A. P., H. J. B. Dick, and R. T. Watkins (1992), Petrogenesis of anomalous K-enriched MORB from the Southwest Indian Ridge: 11°53′ to 14°38′E, *Contrib. Mineral. Petrol.*, *110*, 253–268.

Ligi, M., E. Bonatti, G. Bortoluzzi, G. Carrara, P. Fabretti, D. Penitenti, D. Gilod, A. A. Peyve, S. Skolotnev, and N. Turko (1997), Death and transfiguration of a triple junction in the South Atlantic, *Science*, *276*, 243–245.

Ligi, M., E. Bonatti, G. Bortoluzzi, G. Carrara, P. Fabretti, D. Gilod, A. A. Peyve, S. Skolotnev, and N. Turko (1999), Bouvet Triple Junction in the South Atlantic: Geology and evolution, *J. Geophys. Res.*, *104*(B12), 29,365–29,386.

Lin, J., G. M. Purdy, H. Schouten, J. C. Sempéré, and C. Zervas (1990), Evidence from gravity data for focused magmatic accretion along the Mid-Atlantic Ridge, *Nature*, *344*, 627–632.

Livermore, R. A., and R. J. Hunter (1996), Mesozoic seafloor spreading in the southern Weddell Sea, *Geol. Soc. Spec. Publ.*, *108*(1), 227–241.

Mahoney, J., J. H. Natland, W. M. White, R. Poreda, S. H. Bloomer, R. L. Fisher, and A. N. Baxter (1989), Isotopic and geochemical provinces of the western Indian Ocean spreading centers, *J. Geophys. Res.*, *94*(B4), 4033–4052.

Mahoney, J., A. P. LeRoex, Z. Peng, R. L. Fisher, and J. H. Natland (1992), Southwestern limits of Indian Ocean ridge mantle and origin of low $^{206}Pb/^{204}Pb$ mid-ocean ridge basalt: Isotope systematics of the Central Southwest Indian Ridge (17°–50°E), *J. Geophys. Res.*, *97*(B13), 19,771–19,790.

Marks, K. M., and A. A. Tikku (2001), Cretaceous reconstructions of East Antarctica, Africa and Madagascar, *Earth Planet. Sci. Lett.*, *186*, 479–495.

McAdoo, D., and K. M. Marks (1992), Gravity fields from Geosat and ERS-1 satellite altimetry for geodynamic applications, *Eos Trans. AGU*, *73*, 133.

Mendel, V., and D. Sauter (1997), Seamount volcanism at the super-slow spreading Southwest Indian Ridge between 57°E and 70°E, *Geology*, *25*(2), 99–102.

Mendel, V., D. Sauter, L. Parson, and J.-R. Vanney (1997), Segmentation and morphotectonic variations along a super-slow spreading center: the Southwest Indian Ridge (57°E–70°E), *Mar. Geophys. Res.*, *19*, 505–533.

Mendel, V., D. Sauter, P. Patriat, and M. Munschy (2000), Relationship of the Central Indian Ridge segmentation with the evolution of the Rodrigues triple junction for the past 8 Ma, *J. Geophys. Res.*, *105*(B7), 16,563–16,576.

Mendel, V., D. Sauter, C. Rommevaux-Jestin, P. Patriat, F. Lefebvre, and L. M. Parson (2003), Magmato-tectonic cyclicity at the ultra-slow spreading Southwest Indian Ridge: Evidence from variations of axial volcanic ridge morphology and abyssal hills pattern, *Geochem. Geophys. Geosyst.*, *4*(5), 9102, doi:10.1029/2002GC000417.

Mendel, V., M. Munschy, and D. Sauter (2005), MODMAG, a MATLAB program to model marine magnetic anomalies, *Comput. Geosci.*, *31*, 589–597.

Mével, C., et al. (1997), Sampling the Southwest Indian Ridge: First results of the EDUL cruise (R/V Marion Dufresne II, August 1997), *InterRidge News*, *6*(2), 25–26.

Meyzen, C. M., M. J. Toplis, E. Humler, J. N. Ludden, and C. Mével (2003), A discontinuity in mantle composition beneath the southwest Indian Ridge, *Nature*, *421*, 731–733.

Meyzen, C. M., J. N. Ludden, E. Humler, B. Luais, M. J. Toplis, C. Mével, and M. Storey (2005), New insights into the origin and distribution of the DUPAL isotope anomaly in the Indian Ocean mantle from MORB of the Southwest Indian Ridge, *Geochem. Geophys. Geosyst.*, *6*(11), Q11K11, doi:10.1029/2005GC000979.

Meyzen, C. M., J. Blichert-Toft, J. N. Ludden, E. Humler, C. Mével, and F. Albarède (2007), Isotopic portrayal of the Earth's upper mantle flow field, *Nature*, *447*, 1069–1074.

Michard, A., R. Montigny, and R. Schlich (1986), Geochemistry of the mantle beneath the Rodriguez Triple Junction and the South-East Indian Ridge, *Earth Planet. Sci. Lett.*, *78*, 104–114.

Minshull, T. A., and R. S. White (1996), Thin crust on the flanks of the slow-spreading Southwest Indian Ridge, *Geophys. J. Int.*, *125*, 139–148.

Minshull, T. A., M. R. Muller, and R. S. White (2006), Crustal structure of the Southwest Indian Ridge at 66°E: seismic constraints, *Geophys. J. Int.*, *166*, 135–147.

Mitchell, N. C. (1991a), An evolving ridge system around the Indian Ocean triple junction, *Mar. Geophys. Res.*, *13*, 173–201.

Mitchell, N. C. (1991b), Distributed extension at the Indian Ocean triple junction, *J. Geophys. Res.*, *96*(B5), 8019–8043.

Mitchell, N. C., and L. M. Parson (1993), The tectonic evolution of the Indian ocean triple junction, anomaly 6 to present, *J. Geophys. Res.*, *98*(B2), 1793–1812.

Mitchell, N. C., and R. A. Livermore (1998a), The present configuration of the Bouvet Triple junction, *Geology*, *26*(3), 267–270.

Mitchell, N. C., and R. A. Livermore (1998b), Spiess Ridge: An axial high on the slow spreading Southwest Indian Ridge, *J. Geophys. Res.*, *103*(B7), 15,457–15,471.

Mitchell, N. C., R. A. Livermore, P. Fabretti, and G. Carrara (2000), The Bouvet Triple Junction, 20 to 10 Ma, and extensive transtensional deformation adjacent to the Bouvet and Conrad transforms, *J. Geophys. Res.*, *105*(B4), 8279–8296.

Montési, L. G. J., and M. D. Behn (2007), Mantle flow and melting underneath oblique and ultraslow mid-ocean ridges, *Geophys. Res. Lett.*, *34*, L24307, doi:10.1029/2007GL031067.

Muller, M. R., C. J. Robinson, T. A. Minshull, R. S. White, and M. J. Bickle (1997), Thin crust beneath Ocean Drilling Program borehole 735B at the Southwest Indian Ridge?, *Earth Planet. Sci. Lett.*, *148*, 93–107.

Muller, M. R., T. A. Minshull, and R. S. White (1999), Segmentation and melt supply at the Southwest Indian Ridge, *Geology*, *27*(10), 867–870.

Muller, M. R., T. A. Minshull, and R. S. White (2000), Crustal structure of the South West Indian ridge at the Atlantis II Fracture Zone, *J. Geophys. Res.*, *105*(B11), 25,809–25,828.

Müller, R. D., C. Gaina, A. Tikku, D. Mihut, S. C. Cande, and J. M. Stock (2000), Mesozoic/Cenozoic tectonic events around Australia, in *The History and Dynamics of Global Plate Motions*, *Geophys. Monogr. Ser.*, vol. 121, edited by M. A. Richards et al., pp. 161–188, AGU, Washington, D. C.

Munschy, M., and R. Schlich (1989), The Rodriguez triple junction (Indian Ocean): Structure and evolution for the past one million years, *Mar. Geophys. Res.*, *11*, 1-14.

Munschy, M., and R. Schlich (1990), Etude géophysique des dorsales de l'océan Indien dans la région du point triple de Rodriguez, *Oceanologica Acta*, *10*, 119–128.

Natland, J. H., and H. J. B. Dick (2001), Formation of the lower oceanic crust and the crystallization of gabbroic cumulates at a very slowly spreading ridge, *J. Volcanol. Geotherm. Res.*, *110*, 191–233.

Niu, Y., and M. J. O'Hara (2008), Global correlations of ocean ridge basalt chemistry with axial depth: A new perspective, *J. Petrol.*, *49*(4), 633–664.

Parson, L., E. Gràcia, D. Coller, C. German, and D. Needham (2000), Second order segmentation; the relationship between volcanism and tectonism at the MAR, 38°-35°40′N, *Earth Planet. Sci. Lett.*, *178*, 231–251.

Parson, L. M., D. Sauter, V. Mendel, P. Patriat, and R. C. Searle (1997), Evolution of the axial geometry of the southwest Indian Ocean ridge between the Melville Fracture Zone and the Indian Ocean Triple Junction—Implications for segmentation on very slow-spreading ridges, *Mar. Geophys. Res.*, *19*, 535–552.

Patriat, P., and V. Courtillot (1984), On the stability of the triple junctions and its relation to episodity in spreading, *Tectonics*, *3*, 317–332.

Patriat, P., and L. M. Parson (1989), A survey of the Indian Ocean triple junction trace within the Antarctic plate implications for the junction evolution since 15 Ma, *Mar. Geophys. Res.*, *11*, 89–100.

Patriat, P., and J. Segoufin (1988), Reconstruction of the Central Indian Ocean, *Tectonophysics*, *155*, 211–234.

Patriat, P., J. Segoufin, J. Goslin, and P. Beuzart (1985), Relative positions of Africa and Antarctica in the Upper Cretaceous: Evidence from non-stationary behaviour of fracture zones, *Earth Planet. Sci. Lett.*, *75*, 204–214.

Patriat, P., D. Sauter, M. Munschy, and L. M. Parson (1997), A survey of the Southwest Indian Ridge axis between Atlantis II Fracture Zone and the Indian Triple Junction: Regional setting and large scale segmentation, *Mar. Geophys. Res.*, *19*, 457–480.

Patriat, P., H. Sloan, and D. Sauter (2008), From slow to ultra-slow: A previously undetected event at the Southwest Indian Ridge at ~24Ma, *Geology*, *36*(3), 207–210.

Phipps Morgan, J., E. Parmentier, and J. Lin (1987), Mechanisms for the origin of mid-ocean ridge axial topography: Implications for the thermal and mechanical structure of accreting plate boundaries, *J. Geophys. Res.*, *92*(B12), 12,823–12,836.

Price, R. C., A. K. Kennedy, M. Riggs-Sneeringer, and F. A. Frey (1986), Geochemistry of basalts from the Indian Ocean triple junction: Implications for the generation and evolution of Indian Ocean ridge basalts, *Earth Planet. Sci. Lett.*, *78*, 379–396.

Raitt, R. W. (1963), The crustal rocks, in *The Sea*, edited by M. N. Hill, pp. 85–102, Wiley-Interscience, New York.

Ravilly, M., J. Dyment, P. Gente, and R. Thibaud (1998), Axial magnetic anomaly amplitude along the Mid-Atlantic Ridge between 20°N and 40°N, *J. Geophys. Res.*, *103*(B10), 24,201–24,221.

Reid, I., and H. R. Jackson (1981), Oceanic spreading rate and crustal thickness, *Mar. Geophys. Res.*, *5*, 165–172.

Robinson, C. J., M. J. Bickle, T. A. Minshull, R. S. White, and A. R. L. Nichols (2001), Low degree melting under the Southwest Indian Ridge: The roles of mantle temperature, conductive cooling and wet melting, *Earth Planet. Sci. Lett.*, *188*, 383–398.

Rommevaux-Jestin, C., C. Deplus, and P. Patriat (1997), Mantle Bouguer anomaly along a super-slow spreading ridge: Comparison with central Mid-Atlantic ridge and implications on the accretionary process, *Mar. Geophys. Res.*, *19*, 481–503.

Royer, J. Y., P. Patriat, H. W. Bergh, and C. R. Scotese (1988), Evolution of the Southwest Indian Ridge from the late cretaceous (anomaly 34) to the middle Eocene (anomaly 20), *Tectonophysics*, *155*, 235–260.

Royer, J. Y., R. G. Gordon, and B. C. Horner-Johnson (2006), Motion of Nubia relative to Antarctica since 11 Ma: Implications for Nubia-Somalia, Pacific-North America, and India-Eurasia motion, *Geology*, *34*(6), 501–504.

Salters, V. J. M., and H. J. B. Dick (2002), Mineralogy of the mid-ocean-ridge basalt source from neodymium isotopic composition of abyssal peridotites, *Nature*, *418*, 68–72.

Sandwell, D. T., and W. H. F. Smith (1997), Marine gravity anomaly from Geosat and ERS-1 satellite altimetry, *J. Geophys. Res.*, *102*(B5), 10,039–10,054.

Sauter, D., and V. Mendel (1997), Variations in backscatter strength along the super slow-spreading Southwest Indian Ridge between 57°E and 70°E, *Mar. Geol.*, *140*, 237–248.

Sauter, D., V. Mendel, C. Rommevaux-Jestin, P. Patriat, and M. Munschy (1997), Propagation of the South West Indian Ridge at the Rodrigues triple junction, *Mar. Geophys. Res.*, *19*, 553–567.

Sauter, D., P. Patriat, C. Rommevaux-Jestin, M. Cannat, A. Briais, and the Gallieni Shipboard and Scientific Party (2001), The

Southwest Indian Ridge between 49°15′E and 57°E: Focused accretion and magma redistribution, *Earth Planet. Sci. Lett.*, *192*, 303–317.

Sauter, D., L. M. Parson, V. Mendel, C. Rommevaux-Jestin, O. Gomez, A. Briais, C. Mével, K. Tamaki, and F. S. team (2002), TOBI sidescan sonar imagery of the very slow-spreading Southwest Indian Ridge: Evidence for along-axis magma distribution, *Earth Planet. Sci. Lett.*, *199*, 81–95.

Sauter, D., H. Carton, V. Mendel, M. Munschy, C. Rommevaux-Jestin, J.-J. Schott, and H. Whitechurch (2004a), Ridge segmentation and the magnetic structure of the Southwest Indian Ridge (at 55°30′E, 55°30′E and 66°20′E): Implications for magmatic processes at ultraslow-spreading centers, *Geochem. Geophys. Geosyst.*, *5*, Q05K08, doi:10.1029/2003GC000581.

Sauter, D., V. Mendel, C. Rommevaux-Jestin, L. M. Parson, H. Fujimoto, C. Mével, M. Cannat, and K. Tamaki (2004b), Focused magmatism versus amagmatic spreading along the ultra-slow spreading Southwest Indian Ridge: Evidence from TOBI side scan sonar imagery, *Geochem. Geophys. Geosyst.*, *5*, Q10K09, doi:10.1029/2004GC000738.

Sauter, D., M. Cannat, and V. Mendel (2008), Magnetization of 0–26.5 Ma seafloor at the ultraslow spreading Southwest Indian Ridge 61–67°E, *Geochem. Geophys. Geosyst.*, *9*, Q04023, doi:10.1029/2007GC001764.

Sauter, D., M. Cannat, C. Meyzen, A. Bezos, P. Patriat, E. Humler, and E. Debayle (2009), Propagation of a melting anomaly along the ultra-slow Southwest Indian Ridge between 46°E and 52°20′E: Interaction with the Crozet hot-spot?, *Geophys. J. Int.*, in press.

Sclater, J. G., H. Dick, I. O. Norton, and D. Woodroffe (1978), Tectonic structure and petrology of Antarctic plate boundary near the Bouvet Triple Junction, *Earth Planet. Sci. Lett.*, *37*, 393-400.

Sclater, J. G., R. L. Fisher, P. Patriat, C. R. Tapscott, and B. Parsons (1981), Eocene to recent development of the south-west Indian Ridge, a consequence of the evolution of the Indian Ocean triple junction, *Geophys. J. R. Astron. Soc.*, *64*, 587–604.

Sclater, J. G., N. R. Grindlay, J. A. Madsen, and C. Rommevaux-Jestin (2005), Tectonic interpretation of the Andrew Bain transform fault: Southwest Indian Ocean, *Geochem. Geophys. Geosyst.*, *6*, Q09K10, doi:10.1029/2005GC000951.

Searle, R. C., and A. Bralee (2007), Asymmetric generation of oceanic crust at the ultra-slow spreading Southwest Indian Ridge, 64°E, *Geochem. Geophys. Geosyst.*, *8*, Q05015, doi:10.1029/2006GC001529.

Searle, R. C., K. Fujioka, M. Cannat, C. Mével, H. Fujimoto, and L. M. Parson (1999), FUJI Dome: A large detachment fault near 64°E on the very slow spreading South West Indian Ridge, *Eos Trans. AGU*, *80*(46), Fall Meet. Suppl., Abstract F956.

Ségoufin, J., and P. Patriat (1980), Existence d'anomalies mesozoiques dans le basin de Somalie. Implications pour les relations Afrique-Antarctique-Madagascar, *C. R. Seances Acad. Sci., Ser. B*, *291*, 85–88.

Seyler, M., M. Cannat, and C. Mével (2003), Evidence for major-element heterogeneity in the mantle source of abyssal peridotites from the Southwest Indian Ridge (52° to 69°E), *Geochem. Geophys. Geosyst.*, *4*(2), 9101, doi:10.1029/2002GC000305.

Seyler, M., J. P. Lorand, M. J. Toplis, and G. Godard (2004), Asthenospheric metasomatism beneath the mid-ocean ridge: Evidence from depleted abyssal peridotites, *Geology*, *32*(4), 301–304.

Simonov, V. A., A. A. Peyve, V. Y. Kolobov, A. A. Milosnov, and S. V. Kovyazin (1996), Magmatic and hydrothermal processes in the Bouvet Triple Junction Region (South Atlantic), *Terra Nova*, *8*(5), 415–424.

Sleep, N. H. (1975), Formation of ocean crust: Some thermal constraints, *J. Geophys. Res.*, *80*(29), 4037–4042.

Smith, D. K., J. R. Cann, and J. Escartin (2006), Widespread active detachment faulting and core complex formation near 13°N on the Mid-Atlantic Ridge, *Nature*, *442*, 440–443.

Smith, D. K., J. Escartín, H. Schouten, and J. R. Cann (2008), Fault rotation and core complex formation: Significant processes in seafloor formation at slow-spreading mid-ocean ridges (Mid-Atlantic Ridge, 13°–15°N), *Geochem. Geophys. Geosyst.*, *9*, Q03003, doi:10.1029/2007GC001699.

Sparks, D. W., and E. M. Parmentier (1991), Melt extraction from the mantle beneath spreading centers, *Earth Planet. Sci. Lett.*, *105*, 368–377.

Stamps, D. S., E. Calais, E. Saria, C. Hartnady, J.-M. Nocquet, C. J. Ebinger, and R. M. Fernandes (2008), A kinematic model for the East African Rift, *Geophys. Res. Lett.*, *35*, L05304, doi:10.1029/2007GL032781.

Standish, J. J., H. J. B. Dick, P. J. Michael, W. G. Melson, and T. O'Hearn (2008), MORB generation beneath the ultraslow-spreading Southwest Indian Ridge (9º–25º E): Major element chemistry and the importance of process versus source, *Geochem. Geophys. Geosyst.*, *9*, Q05004, doi:10.1029/2008GC001959.

Tucholke, B. E., J. Lin, and M. C. Kleinrock (1998), Megamullions and mullion structure defining oceanic metamorphic core complexes on the Mid-Atlantic Ridge, *J. Geophys. Res.*, *103*(B5), 9857–9866.

Tucholke, B. E., M. D. Behn, W. R. Buck, and J. Lin (2008), Role of melt supply in oceanic detachment faulting and formation of megamullions, *Geology*, *36*(6), 455–458.

Wang, X., and J. R. Cochran (1995), Along-axis gravity gradients at mid-ocean ridges: Implications for mantle flow and axial morphology, *Geology*, *23*(1), 29–32.

Wessel, P., and W. H. F. Smith (1995), New version of Generic Mapping Tools released, *Eos Trans. AGU*, *76*, 329.

West, B. P., H. Fujimoto, C. Honsho, K. Tamaki, and J.-C. Sempéré (1995), A three-dimensional study of the Rodrigues triple junction and Southwest Indian Ridge, *Earth Planet. Sci. Lett.*, *133*, 175–184.

White, R. S., T. A. Minshull, M. J. Bickle, and C. J. Ronbinson (2001), Melt generation at very slow-spreading oceanic ridges: Constraints from geochemical and geophysical data, *J. Petrol.*, *42*(6), 1171–1196.

M. Cannat, Laboratoire de Géosciences Marines, CNRS-UMR7097, Institut de Physique du Globe, 4 Place Jussieu, F-75252 Paris cedex 05, France. (cannat@ipgp.jussieu.fr)

D. Sauter, Institut de Physique du Globe de Strasbourg, UMR7516 CNRS-UdS, Ecole et Observatoire des Sciences de la Terre, 5 rue Descartes, F-67084 Strasbourg cedex, France. (daniel.sauter@eost.u-strasbg.fr)